

# Performance of two Askaryan Radio Array stations and first results in the search for ultra-high energy neutrinos

Allison, P.,<sup>1,2</sup> Bard, R.,<sup>3</sup> Beatty, J. J.,<sup>1,2,4</sup> Besson, D. Z.,<sup>5,6</sup> Bora, C.,<sup>7</sup> Chen, C.-C.,<sup>8</sup> Chen, C.-H.,<sup>8</sup> Chen, P.,<sup>8</sup> Christenson, A.,<sup>9</sup> Connolly, A.,<sup>1,2</sup> Davies, J.,<sup>10</sup> Duvernois, M.,<sup>9</sup> Fox, B.,<sup>11</sup> Gaior, R.,<sup>12</sup> Gorham, P. W.,<sup>11</sup> Hanson, K.,<sup>13</sup> Haugen, J.,<sup>9</sup> Hill, B.,<sup>11</sup> Hoffman, K. D.,<sup>3</sup> Hong, E.,<sup>1,2</sup> Hsu, S.-Y.,<sup>8</sup> Hu, L.,<sup>8</sup> Huang, J.-J.,<sup>8</sup> Huang, M.-H. A.,<sup>8</sup> Ishihara, A.,<sup>12</sup> Karle, A.,<sup>9</sup> Kelley, J. L.,<sup>9</sup> Kennedy, D.,<sup>5</sup> Kravchenko, I.,<sup>7</sup> Kuwabara, T.,<sup>12</sup> Landsman, H.,<sup>14</sup> Landrie, A.,<sup>9</sup> Li, C.-J.,<sup>8</sup> Liu, T. C.,<sup>8</sup> Lu, M.-Y.,<sup>9</sup> Macchiarulo, L.,<sup>11</sup> Mase, K.,<sup>12</sup> Meures, T.,<sup>13,\*</sup> Meyhandan, R.,<sup>11</sup> Miki, C.,<sup>11</sup> Morse, R.,<sup>11</sup> Nam, J.,<sup>8</sup> Nichol, R. J.,<sup>10</sup> Nir, G.,<sup>14</sup> Novikov, A.,<sup>6</sup> Pfendner, C.,<sup>1,2</sup> Ratzlaff, K.,<sup>15</sup> Relich, M.,<sup>12</sup> Richman, M.,<sup>3</sup> Ritter, L.,<sup>11</sup> Rotter, B.,<sup>11</sup> Sandstrom, P.,<sup>9</sup> Schellin, P.,<sup>1,2</sup> Shultz, A.,<sup>7</sup> Seckel, D.,<sup>16</sup> Shiao, Y.-S.,<sup>8</sup> Stockham, J.,<sup>5</sup> Stockham, M.,<sup>5</sup> Touart, J.,<sup>3</sup> Varner, G. S.,<sup>11</sup> Wang, M.-Z.,<sup>8</sup> Wang, S.-H.,<sup>8</sup> Yang, Y.,<sup>13</sup> Yoshida, S.,<sup>12</sup> and Young, R.<sup>15</sup>  
(The ARA collaboration)

<sup>1</sup>*Dept. of Physics, The Ohio State University, 191 West Woodruff Avenue, Columbus, OH, USA*

<sup>2</sup>*Center for Cosmology and Astro-Particle Physics,  
The Ohio State University, 191 West Woodruff Avenue, Columbus, OH, USA*

<sup>3</sup>*Dept. of Physics, Univ. of Maryland, College Park, MD, USA*

<sup>4</sup>*Department of Astronomy, The Ohio State University,  
4055 McPherson Laboratory, 140 West 18th Avenue, Columbus, OH, USA*

<sup>5</sup>*Dept. of Physics and Astronomy, Univ. of Kansas, Lawrence, KS, USA*

<sup>6</sup>*National Research Nuclear University, Moscow Engineering Physics Institute, Moscow, Russia*

<sup>7</sup>*Dept. of Physics and Astronomy, Univ. of Nebraska-Lincoln, NE, USA*

<sup>8</sup>*Dept. of Physics, Grad. Inst. of Astrophys., & Leung Center for  
Cosmology and Particle Astrophysics, National Taiwan Univ., Taipei, Taiwan*

<sup>9</sup>*Dept. of Physics and Wisconsin IceCube Particle Astrophysics Center, University of Wisconsin, Madison, WI, USA*

<sup>10</sup>*Dept. of Physics and Astronomy, Univ. College London, London, United Kingdom*

<sup>11</sup>*Dept. of Physics and Astronomy, Univ. of Hawaii, Manoa, HI, USA*

<sup>12</sup>*Dept. of Physics, Chiba University, Tokyo, Japan*

<sup>13</sup>*Université libre de Bruxelles - Interuniversity Institute for High Energies (IIHE), Belgium*

<sup>14</sup>*Weizmann Institute of Science, Rehovot, Israel*

<sup>15</sup>*Instrumentation Design Laboratory, Univ. of Kansas, Lawrence, KS, USA*

<sup>16</sup>*Dept. of Physics and Astronomy, Univ. of Delaware, Newark, DE, USA*

Ultra-high energy neutrinos are interesting messenger particles since, if detected, they can transmit exclusive information about ultra-high energy processes in the Universe. These particles, with energies above  $10^{16}$  eV, interact very rarely. Therefore, detectors that instrument several gigatons of matter are needed to discover them. The ARA detector is currently being constructed at South Pole. It is designed to use the Askaryan effect, the emission of radio waves from neutrino-induced cascades in the South Pole ice, to detect neutrino interactions at very high energies. With antennas distributed among 37 widely-separated stations in the ice, such interactions can be observed in a volume of several hundred cubic kilometers. Currently 3 deep ARA stations are deployed in the ice of which two have been taking data since the beginning of the year 2013. In this publication, the ARA detector “as-built” and calibrations are described. Furthermore, the data reduction methods used to distinguish the rare radio signals from overwhelming backgrounds of thermal and anthropogenic origin are presented. Using data from only two stations over a short exposure time of 10 months, a neutrino flux limit of  $3 \times 10^{-6}$  GeV/cm<sup>2</sup>/s/sr is calculated for a particle energy of  $10^{18}$  eV, which offers promise for the full ARA detector.

## I. INTRODUCTION

In 1966 Greisen, Zatsepin and Kuzmin predicted an interaction of ultra-high energy cosmic rays (**UHECRs**) with the recently discovered cosmic microwave background radiation [1, 2]. In such interactions, pions are produced resonantly which subsequently decay into neutrinos, as first postulated by Berezhinsky and Zatsepin in

1968 [3]. Due to the contribution of the Delta resonance to the cross section for this interaction, UHECRs are unable to reach us from sources on cosmological distance scales, i. e. beyond tens of Mpc, which implies a sharp cutoff in the cosmic ray spectrum at an energy of around  $10^{19.5}$  eV. Such a cutoff has indeed been confirmed by the largest cosmic ray air shower detectors Telescope Array [4] and the Pierre Auger Observatory [5]. However, the lack of UHECRs arriving at Earth could be due to a number of underlying reasons dependent on their properties. The mass composition, for example, plays a crucial role

\* thomas.meures@icecube.wisc.edu

in determining the dominant energy loss for UHECRs [6]. Furthermore, this energy loss is influenced by the distribution of sources and the primary energy spectrum of cosmic rays.

As a consequence, the neutrino flux depends strongly on all three parameters, the UHECR composition, their energy spectrum and their source distribution, and a measurement of this flux can be used to place constraints on them. Moreover, due to the GZK effect and similar absorption mechanisms for HE gamma rays, neutrinos are the only feasible known particles for the study of UHE sources more distant than a few tens of Mpc. Neutrinos, chargeless and only weakly interacting with extremely low cross sections, arrive at detectors unscattered and undeflected by intervening particles and fields and they may be correlated to UHE sources at the furthest distances in the Universe.

The expected flux of GZK neutrinos at Earth from different cosmic ray models is very low [7] and, in combination with the low interaction cross section [8], leads to an interaction rate of less than 1 GZK neutrino per gigaton of matter per year. Therefore, large detectors, covering several hundred cubic kilometers of water equivalent matter are needed to record neutrino events in sufficient quantity to investigate their flux.

The large attenuation length of Antarctic ice to radiofrequency waves, on the order of 1 km for frequencies around 500 MHz [9], opens the possibility to instrument detection volumes of comparable scale by utilizing coherent radio emission from neutrino induced cascades in radio transparent media; the so-called Askaryan effect [10, 11]. In the interactions of high energy neutrinos with electrons or nuclear matter, electromagnetic (EM) cascades are produced which build up a net negative charge of roughly 20% close to the shower maximum. This imbalance originates mainly from Compton scattering of cascade photons on atomic electrons with smaller contributions from other ionizing effects like positron annihilation with atomic electrons [12, 13]. The net charge acts as a moving current and emits electromagnetic waves, which become coherent at wavelengths comparable to the lateral cascade dimensions. This is valid in the radio regime. In the case of coherent emission, the strength of the EM far field is proportional to the cascade energy. The Askaryan effect has been verified with photon and electron beams directed into sand, salt and ice targets [14–16].

Askaryan radiation is a consequence of a neutrino of any flavour interacting in a radiotransparent medium such as ice, however, as the effect ultimately comes from the induced EM cascade, the detection efficiency is strongly dependent on neutrino flavor. Charged-current  $\nu_e$  interactions and  $\nu_e + e^-$  elastic scatters convert a large fraction of the neutrino energy into the EM cascade. These interactions are mostly available to electron neutrinos. Neutral-current interactions of all  $\nu$  flavors may initiate hadronic cascades which receive, on average, only 20% of the neutrino energy. These hadronic cascades will

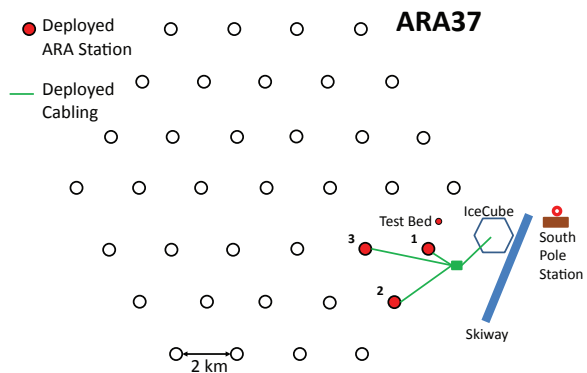


Figure 1. An area map of the planned ARA detector at South Pole. The stations are indicated by the black circles. Red filled circles denote the currently deployed stations.

themselves produce EM sub-cascades due principally to decaying  $\pi^0$  particles, however a fraction of energy is lost to hadrons. On the other hand very high energy EM cascades undergo elongation via the LPM effect [17, 18] which does not affect hadronic cascades. Radiation emitted by the LPM-elongated EM cascades is more strongly beamed at the Cherenkov angle and thus is less likely to intersect detection antennas. Thus, overall, despite their stronger signal emission, statistically speaking,  $\nu_e$  are not necessarily the dominant detected flavor given an astrophysical expectation of  $(\nu_e : \nu_\mu : \nu_\tau) = (1 : 1 : 1)$ .

## II. THE INSTRUMENT

The Askaryan Radio Array (ARA) is a neutrino detector, currently under construction at the geographic South Pole next to the IceCube experiment. It is designed to utilize the Askaryan effect to detect interactions of GZK neutrinos in the South Polar ice sheet. At the chosen site thousands of square kilometers of ice with a thickness of about 3 km are available to act as a radio transparent detector medium and to allow for the construction of a  $\mathcal{O}(100 \text{ Gt})$  detector. Due to its low temperature between  $-55^\circ\text{C}$  and  $-30^\circ\text{C}$  in the top 2 km [19], the South Pole ice sheet has low radio attenuation. On average, an attenuation length of 820 m integrated over the top 2 km of ice has been measured for frequencies around 500 MHz [9]. Furthermore, the Amundsen-Scott station provides the infrastructure to support large projects such as the ARA experiment.

### A. General design

The ARA detector baseline consists of 37 antenna clusters (“stations”) spaced by 2 km in a hexagonal grid (Figure 1). Each station is designed to operate as an autonomous neutrino detector and simulations have shown

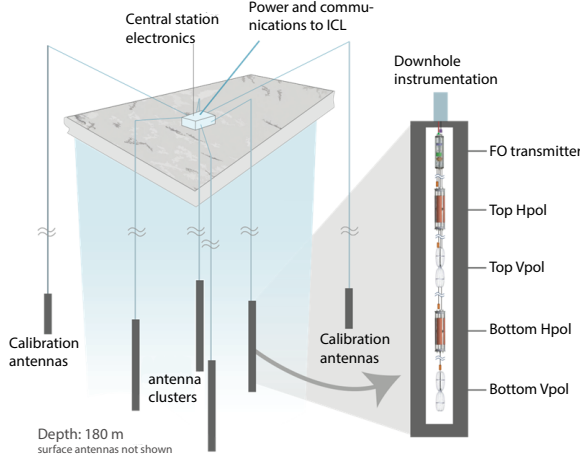


Figure 2. The baseline design of an ARA station with a zoom into the string details and a view of the deployed antennas of both polarization.

a distance of 2 km to nearly maximize the array’s effective area at  $10^{18}$  eV [9].

Each station comprises 16 measurement antennas, deployed on strings in groups of 4 at the bottom of 200 m deep holes. In the baseline design, these antennas form a cube of 20 m at each side (Figure 2). This design is in the process of being optimized based on analysis results from the first ARA stations and simulations. Each hole contains two antennas of horizontal and two antennas of vertical polarization, all recording data between 150 MHz and 850 MHz. Two separated polarizations are chosen to be able to determine the polarization of the incoming signal, which is important for neutrino reconstruction. The antenna names are composed of the string number as  $D\#$ , their position on the string ( $T$  for top,  $B$  for bottom) and their polarization ( $V$  for vertical,  $H$  for horizontal).

The antennas are deployed at depths between 170 m and 190 m to minimize the effects of ray-tracing in the ice. Due to the depth-dependence of the temperature and density of the South Pole ice sheet, the index of refraction changes with depth [20]. This effect is strongest in the top 200 m, starting from an index of 1.35 at the surface and changing to a value of 1.78 for the deep ice at a depth of roughly 200 m. As described in [9, 21], this causes the path of radio rays to be bent downwards which renders vertex reconstructions difficult. Moreover, a shadowed area is produced, from which signals can not reach shallowly deployed antennas, thus reducing effective neutrino volume. Therefore, a deep deployment of the antennas is favorable.

In addition to the receiver channels, 4 calibration antennas, which transmit pulses for calibration of the station timing, geometry, and signal efficiency, are deployed on two extra strings. They are positioned at a distance of about 40 m to the station core at a similar depth as the measurement antennas. Each hole contains one antenna

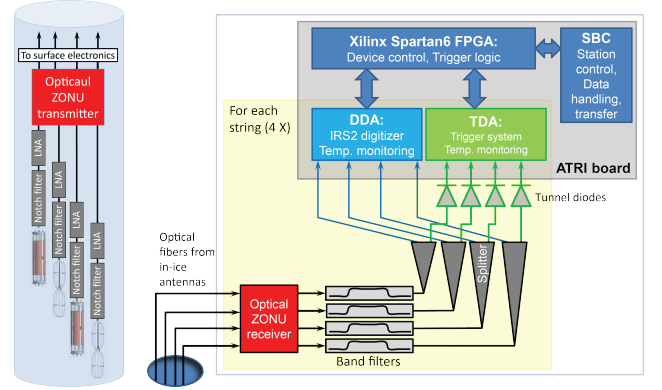


Figure 3. **(Left)** The components of the down-hole signal chain on each string in the ARA stations. **(Right)** The surface Data acquisition system of the ARA stations, showing the most important components. Components framed in yellow are common to all strings.

of each polarization.

The antennas used in ARA are birdcage dipoles for the vertical polarization (**Vpol**) and ferrite loaded quad-slot antennas for the horizontal polarization (**Hpol**). Given the drilled antenna holes with a diameter of only 15 cm, the design of Hpol antennas with reasonable sensitivity down to 150 MHz is very challenging. Slotted copper cylinders show reasonable low-frequency performance with a voltage standing wave ratio below 3, for frequencies above 300 MHz [9]. This can be further improved by adding ferrite material in the cylinder core.

The signal recorded by the antennas is first filtered by a bandpass and notch filter, to reject frequencies of low antenna sensitivity and narrow-band communications. After filtering, the signal is amplified by Low Noise Amplifiers (**LNAs**) and transmitted analog to the surface through fiber cables via optical ZONU links (Figure 3(a)). At the surface, the signal is filtered again, split and fed to the trigger system as well as to the digitization system (Figure 3(b)). A first calibration of the full signal chain and antenna response after deployment in the ice can be found in Section IID.

In the trigger system, the signal is processed by an integrating tunnel diode, producing energy envelopes of the incoming waveforms, which can be processed in the trigger electronics mounted on the Triggering Daughter board for ARA (**TDA**). On this board, the signal is read into the digital electronics and a trigger may be formed, depending on whether the event satisfies the conditions required in the trigger logic implemented in an FPGA. This logic is currently a simple multiplicity trigger, requiring signal on 3 out of 8 channels of one polarization. Investigations are currently being performed to replace this with a smarter algorithm which provides more efficient background rejection and better signal retention.

The digitization system is located on the Digitizing Daughter board for ARA (**DDA**). In this system the data is sampled by the IRS2 ASIC, a digitization chip

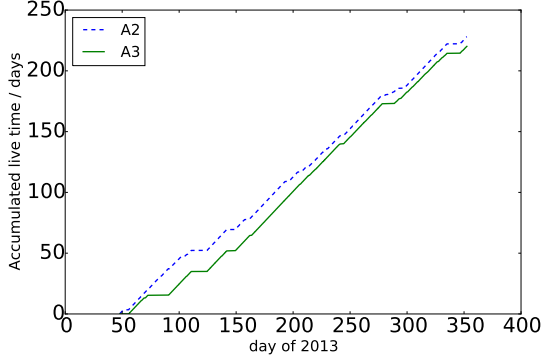


Figure 4. The accumulated live time of stations A2 and A3 in 2013. Horizontal line segments indicate extended downtimes of the detectors.

capable of sampling data at a rate of 4 GS/s. In the ARA detector, the sampling speed is tuned to 3.2 GS/s. The IRS2 chip contains 8 channels each with a 32k-element Switched Capacitor Array (**SCA**). The 32k elements are further subdivided into 512 randomly write-addressable blocks of 64 samples each. Analog sampling is continuous and is stopped by an external trigger to signal the start of digitization and readout of the analog storage blocks of interest. Performance of this early version of SCAs with deep analog storage buffers shows promise for multichannel high-speed, low-power samplers. Power consumption is in the range of 20 mW per channel. In principle deadtimeless operation is possible due to the deep analog buffer, however noise issues related to simultaneous readout and digitization have prevented operation in this mode to date. The calibration of this digitizer is presented in Appendix A.

Both the TDA and DDA board are mounted on the ARA Triggering and Readout Interface (**ATRI**) which provides all logic for the data acquisition systems in a single Spartan-6 FPGA. This FPGA is programmed by, and exchanges its data with, an Intel atom-based Single Board Computer (**SBC**) which handles the data transfer to storage on discs in the IceCube Laboratory (**ICL**). Currently an event rate of 5 Hz can be accommodated on a USB link between the FPGA and the SBC. Future upgrades for this link envision a much higher bandwidth PCI-express bus to increase the total station trigger rate.

The ARA detector in its current status consists of 3 stations, of which two were taking data in the year 2013 and produced the data for this analysis.

## B. Performance of the ARA stations A2 and A3

The first data from the deep ARA detector have been recorded by stations A2 and A3. Station A1 could not deliver data in the year 2013 due to an issue in the communications system. We plan to fix this problem in the 2015-2016 Antarctic summer season.

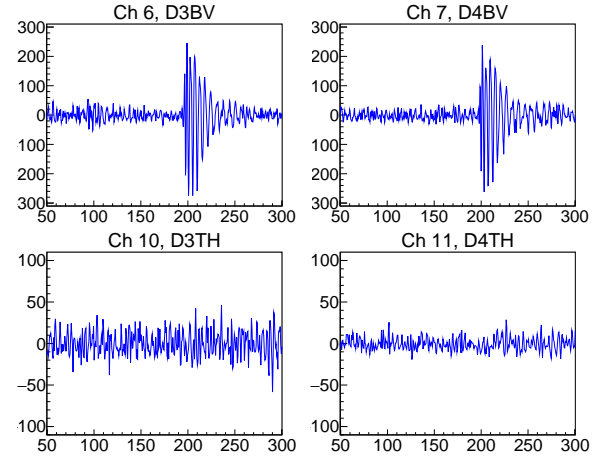


Figure 5. Vpol pulser signal recorded by station A3 for 4 example antennas, displayed in mV versus ns. As is evident, the polarization separation is very clean and only Vpol antennas show any response.

The positions of the two stations, as embedded in the full ARA37 design, are shown in Figure 1. Their structure closely follows the ARA baseline design as described in Section II A. After being deployed in February 2013, the stations recorded 10 months of data until the end of that year (Figure 4). Due to various infrastructural issues and optimizations that interrupted the detector operation, there were several extended periods of down time, sometimes lasting for days. Therefore, the two detectors were only running 75% of the time and correspondingly accumulated about 228 (A2) and 220 (A3) days of live time during those months. Meanwhile, station operation has become more stable through debugging and optimization of the data acquisition (**DAQ**) firmware and software and through the development of new monitoring tools which allow us to identify and solve problems within a few hours. This resulted in a significant rise in live time for the year 2014. The dead time during operations due to digitizer occupancy and the limited data transfer bandwidth is very small and less than 1% of the total run-time.

Of the 32 deep in-ice measurement channels in the two stations, 31 are fully operational. The bottom Hpol channel on string 4 (D4BH) in A2 shows strong noise fluctuations which are believed to be due to a damaged LNA. Figure 5 shows a Vpol pulser waveform as recorded by A3. One can see the fully operational Vpol antennas. Because of the polarization of the signal, the pulser is not observed in the Hpol antennas. The RMS of the background noise on the two stations is relatively stable throughout the year, as it is shown for A2 in Figure 6.

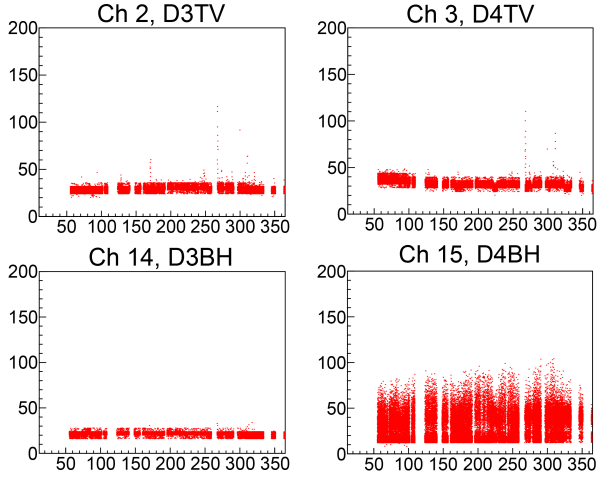


Figure 6. The RMS of events recorded by 4 selected measurement channels from A2 in 2013, plotted in mV versus the day of 2013. The large variation observed in channel D4BH is indicative of failure of that particular channel.

### C. The calibration of station geometry and timing

After having achieved a stable timing from the digitizer chip, the systematic errors in this timing and the precise positions of the antennas in a station need to be determined, to allow for accurate vertex reconstructions. The antennas are suspended on four strings in four vertical holes, connected by stiff cables. Their XY-coordinates can thus be assumed to coincide within one hole. Furthermore, the vertical distances and the cable delays have been measured and are assumed to be correct with a negligible error. Parameters which still need to be calibrated are the position of each string and the relative time delay between them. Considering that one string has to be chosen as perfectly positioned and the rotation of the station around this string to be fixed to get a well determined system, one needs to calibrate 17 remaining parameters of positions and cable delays.

Such calibration is performed by using calibration pulser signals and determining the arrival time difference between signals on different antennas. For this quantity and the geometrical positions of the antennas one can set up an equation for each possible antenna pair and for all 4 pulsers. Considering the two polarizations, a system of 28 independent equations can be constructed. For these equations we can set up a  $\chi^2$  value as

$$\chi^2 = \sum [c^2(dt_{k,i,ref}^2 - dt_{k,j,ref}^2 + x_k \cdot 2x_{ij} + y_k \cdot 2y_{ij} + z_k \cdot 2z_{ij} - t_{k,ref} \cdot 2c^2 dt_{k,i,j} - r_i^2 + r_j^2)]. \quad (1)$$

Here we use  $c = 0.3/1.755$  m/ns as the speed of light in ice at the average antenna depth, taken from [20]. The coordinates of the pulsers are denoted by  $x, y, z$  and the arrival time difference by  $dt$ , with the subscripts  $k$

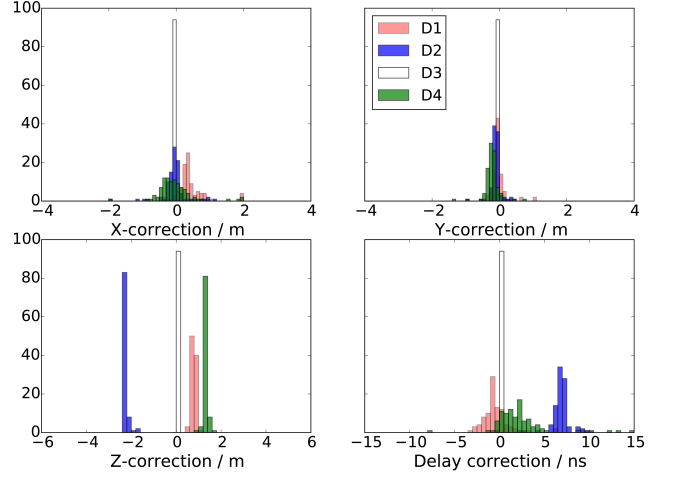


Figure 7. Results of the fits for the geometrical and timing calibration of the strings in station A3. Note that string D3 has been used as the reference and is fixed in the  $\chi^2$ -minimization of this calibration.

for the used pulser and  $i, j$  for the respective antennas. The parameter  $r$  indicates the distance of the antenna to the station center. This  $\chi^2$  is minimized with standard minimizer tools. This procedure is performed multiple times and the average of the outcomes is taken as the final result. Figure 7 shows how different parameters are constrained by this method for station A3. It becomes apparent that the current geometrical setup is strongest in determining the string depth while the constraints on the X- and Y-position, and the inter-string delays are relatively weak.

The result of this calibration is checked via the reconstruction of an independent pulsing antenna, mounted at a distance of about 4 km from both ARA stations on the rooftop of the IceCube Laboratory. The reconstruction algorithm described in Section IV B is used for this cross check. The figures of merit are the stability of the reconstruction as well as the residual which indicates the internal consistency of the station geometry. Signals from the rooftop pulser are not tagged as such and have to be filtered out of all recorded data by other means. The residual is plotted before and after calibration for all data recorded during a rooftop pulser run in Figure 9. Two peaks are visible in this distribution: one for noise waveforms with high residual around  $10^{-1.5}$  and one for signal which shifts to significantly lower values after the calibration. This indicates that the assumed geometry is more consistent with the measured timing after the calibration has been applied. Figure 8 shows the actual result of the reconstruction compared to the expected value. After calibration, the reconstruction is much more self-consistent than before. Currently, more measurements are being taken to further improve the precision of this calibration.



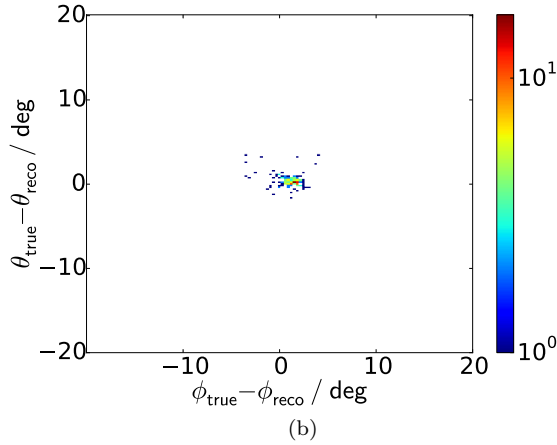
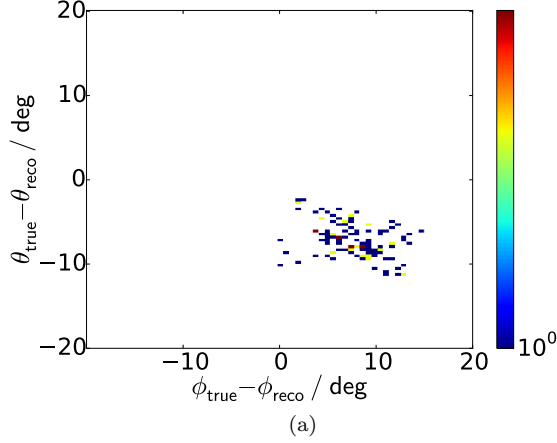


Figure 8. The directional rooftop pulser reconstruction with A3 (a) before and (b) after the geometrical calibration. The axes show the difference to the expected azimuth  $\phi_{\text{true}}$  (X-axis) and the expected zenith  $\theta_{\text{true}}$  (Y-axis). Reconstruction quality criteria are only applied loosely. It should be noted that the data from the rooftop pulser are not part of the calibration data sample.

#### D. Signal chain calibration

In the amplitude calibration of the ARA signal chain, we try to determine the noise temperature of the environment, the noise figure of the signal chain and the directional gain of the antenna.

The total noise temperature seen by an ARA antenna has been calculated to be  $T_{\text{ant}} = 247 \pm 13$  K for Vpol and to  $T_{\text{ant}} = 249 \pm 13$  K for Hpol antennas at 300 MHz, based on information from [9, 22, 23]. This includes contributions from the atmosphere and galactic center and also accounts for the temperature and attenuation profile of the ice.

The calibration of the signal chain is particularly challenging since the deployment of fixed strings in 200 m deep holes allows neither a detailed investigation of the directional gain pattern of the antenna nor noise figure

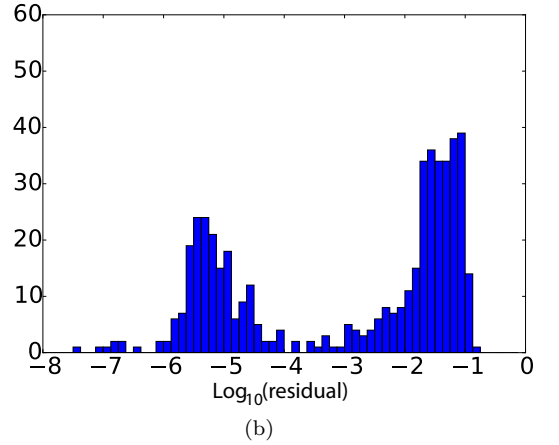
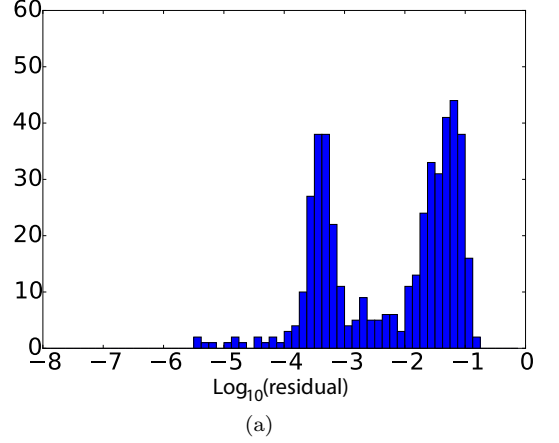


Figure 9. The residual of the rooftop pulser reconstruction with A3 (a) before and (b) after the geometrical calibration. The bimodal distributions contain noise events with a residual of roughly  $10^{-1.5}$  and signal with lower residuals which is reduced after the calibration.

measurements *in-situ*.

The noise factor  $F$  of the signal chain has been measured for each channel at the surface at room temperature prior to deployment. This noise factor is used to calculate the noise temperature of the signal chain. The change due to the signal chain being lowered into the ice with a local environmental temperature of roughly 220 K is estimated as a linear change with ambient temperature. The total noise contribution depends on the transmission coefficient of the antenna. For perfect coupling it can be calculated to (e.g., at 300 MHz):

$$\begin{aligned} T_{\text{tot}} &= T_{\text{ant}} + T(180 \text{ m}) \cdot (F - 1) \\ &= 247 \text{ K} + 220 \text{ K} \cdot (1.6 - 1) = 379 \text{ K}. \end{aligned} \quad (2)$$

With knowledge of this noise floor, the directional gain can be determined using the external noise sources at each station. These sources are noise diodes, connected to the pulser antennas, installed in the vicinity of the ARA stations. Under the assumption that all installed

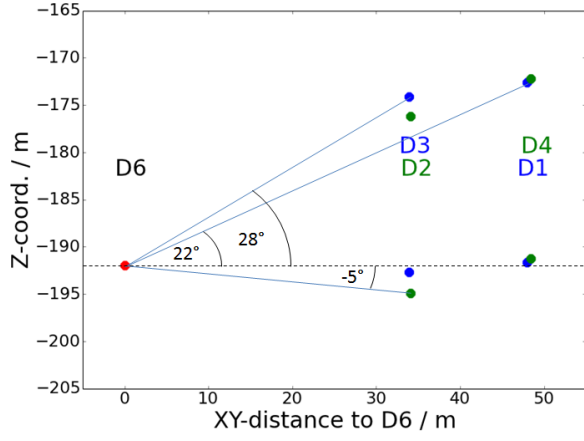


Figure 10. The relative geometry of the Vpol antennas to the D6 pulser in A3.

antennas of the same polarization have the same angular gain pattern, the geometric relation between the pulsers and all 8 measurement antennas of one polarization in both stations can be used to measure the gain pattern for different angles. For this measurement, we assume further that the directionality in azimuth is isotropic. With the available antennas we can establish 24 different relations in elevation which are however clustered at certain angles, as shown on the example of A3 in Figure 10. The antenna directivity  $D$  at a given angle is then calculated via the Friis transmission equation [24] and the known noise factor from

$$\sqrt{D_r D_t} = \frac{4\pi R}{\lambda} \sqrt{\frac{P_{out} - N_{out}}{t_r t_t P_t N_{out}}} \cdot \sqrt{(N_{ant} + 220 \text{ K} \cdot (F - 1))}, \quad (3)$$

with  $N_{ant}$  the power corresponding to  $T_{ant}$ ,  $t$  the transmission coefficient between the antenna and the signal chain,  $P_t$  the input power to the noise source antenna and  $R$  the distance between transmitter and receiver antennas.  $N_{out}$  is the measured output power without any applied signal and  $P_{out}$  denotes the total recorded power when a measurable fluctuation occurs in the given noise environment. These are the experimentally measured values.

The transmission coefficient  $t$  is taken from XFDTD simulations [25] of the deployed antennas in ice. These simulations are precise to about 10%. For the directivity, we assume for now  $D_r = D_t = D$ , for a transmitter and receiver of the same polarization.

The antenna gain can then be calculated as

$$G = D \cdot t. \quad (4)$$

Figure 11 shows the gain measured for the A3 Vpol antennas with a noise diode signal from the D6 pulser plotted with systematic errors, which are dominant in this measurement. The comparison to simulations shows that measurements beyond 450 MHz are not very reliable. This is mainly due to the low signal strength at

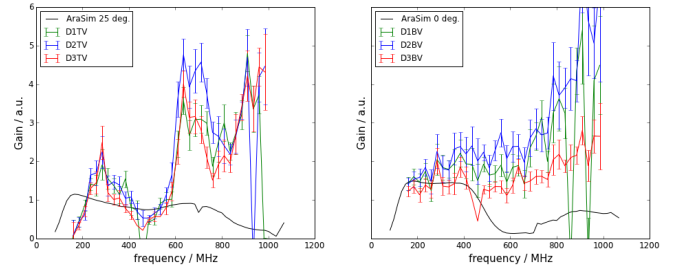


Figure 11. The directional gain results (linear scale) in A3 for all Vpol antennas compared to the current simulation (black line) at the main reception angles (see Figure 10) plotted versus frequency. The labels show the string number  $D\#$  and the position on the string ( $TV$  for top Vpol,  $BV$  for bottom Vpol).

those frequencies, which is expected due to the low sensitivity of the signal chain at high frequencies. Such behavior allows for a stronger influence of non-linear effects in this region which are difficult to quantify. Their influence, however, on the frequency range below 450 MHz, given sufficient signal strength, is very small. The geometrical relation between the antennas is shown in Figure 10.

Figure 12 shows the gain measured by all possible antennas versus the reception angle. As is evident, the antennas are unfortunately not distributed equally over the angular range, but concentrated at a few points. Therefore, it is difficult to make a prediction for the full angular response. The gain pattern currently used in the ARA simulation (Section III) is included in Figure 12 for comparison. This simulation has been derived for a Vpol antenna in ice as an adapted NEC2 simulation. For the frequency range between 200 MHz and 400 MHz, the measurements show rough consistency with simulations within the systematic uncertainties, which amount to roughly 30%. This systematic uncertainty is

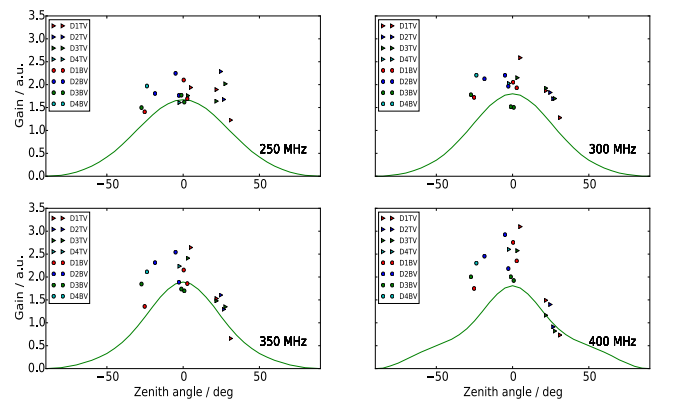


Figure 12. The directional gain results versus reception angle from A2 and A3 for all Vpol antennas compared to the current simulation (green line) at different frequencies. All data is normalized to an isotropic directionality pattern.

mainly induced by the limited knowledge of the strength of the noise sources used. The large disagreement between measurement and simulations for frequencies beyond 500 MHz still needs investigation. However, it does not have a strong influence on the waveforms since, due to the sensitivity properties of the signal chain, roughly 90% of the signal power is recorded below 500 MHz.

### III. SIMULATIONS

The simulation of neutrino vertices for ARA is performed with the AraSim code, which is described in detail in [21, 26]. In this section a short summary of the simulation is presented.

In AraSim, forced neutrino interactions are generated at uniformly distributed locations in a cylindrical volume. This volume is centered on the simulated ARA station with incoming neutrino directions uniform in  $\cos\theta$ . It is bounded by the bedrock under the ice in depth and by an energy dependent radius, chosen to include all possibly triggering events. For each interaction, a weight is calculated based on the probability that the neutrino would interact at the given point after having passed earthbound material along its trajectory. This probability depends on the energy dependent cross-section for a neutrino interaction [27] and the summed number of radiation lengths along the neutrino path. The primary neutrino energy spectrum can be chosen freely.

For each simulated neutrino interaction, a cascade and its radio frequency emission are modeled from theoretical approximations. The results obtained in the following analysis are based on modeling of the Askaryan emission in the frequency domain according to [13], which has since been updated to a semi-analytical method of simulating the emission for each event based on [28].

The trajectory of the RF signal to the antenna is calculated using fitted models for the index of refraction [20] and the final signal strength is derived taking into account the depth dependent attenuation length [9].

Finally, the signal chain and the trigger system are modeled after calibration measurements of their components in the laboratory. For the antenna response, a NEC2 simulation is used. The trigger logic is modeled in AraSim as it is currently set up in the ARA stations: whenever 3 out of 8 antennas of the same polarization cross a given threshold, an event is recorded.

Thermal background noise is modeled using the average frequency spectrum from unbiased forced trigger events recorded throughout 2013, measured with each antenna in station A3. The production of a significant sample of thermal noise data is difficult due to the  $6\sigma$  power-threshold which is currently used in the trigger system to limit the event rate to 5 Hz. Therefore, simulated noise is exclusively used to develop and initially test algorithms while final checks and the estimation of background are performed on recorded data.

From simulations, the effective area of the two ARA

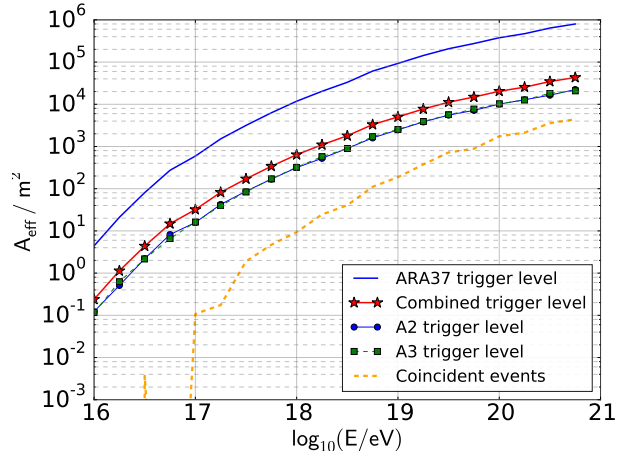


Figure 13. The effective area of the two ARA stations as a function of neutrino energy.

stations can be calculated at the trigger level to be:

$$A_{\text{eff}}(E) = \frac{V_{\text{gen}}(E)}{N_{\text{gen}}(E)} \frac{1}{L_{\text{int}}(E)} \cdot \sum_{i, \text{trig}} \omega_i, \quad (5)$$

where  $V_{\text{gen}}$  is the cylindrical volume over which events are generated,  $N_{\text{gen}}$  is the number of events which have been generated,  $\omega_i$  is the weight of each event  $i$  which triggered the detector and  $L_{\text{int}}$  is the interaction length at the given energy. The effective area for the combined A2 and A3 detector is plotted at the trigger level in Figure 13. In this plot, also the single effective areas per station are shown as well as the effective area for events which are coincident to both stations. These coincidences amount to roughly 5% of all events at an energy of  $10^{18}$  eV.

### IV. DATA ANALYSIS

The analysis of the first 10 months of A2 and A3 data has been optimized for sensitivity to neutrino interactions at a fixed rejection of thermal and anthropogenic backgrounds.

The ARA detector records events at a rate of roughly 5 Hz. These events are mostly thermal noise and to a lesser degree, backgrounds of anthropogenic origin. In this analysis these backgrounds are reduced in two steps: with a thermal noise filter and by application of angular cuts to reconstructed vertices. All algorithms have been developed and tested on a 10% subset of the full recorded data, to avoid a bias in the analysis. Cuts are developed to reduce the expected background to a factor 10 beneath the level of expected neutrino events. After the cuts are finalized, the analysis is applied to the full recorded data set for the year 2013.



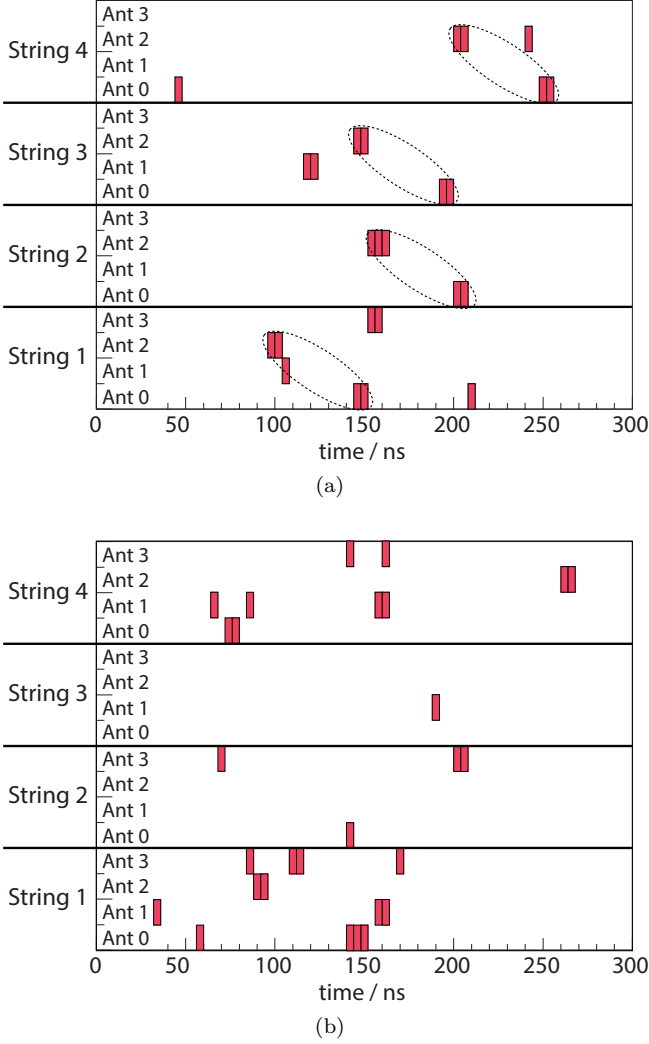


Figure 14. **(a)** The hit pattern for a simulated event containing a signal waveform. The hits are indicated by the colored squares. Hits which correspond to the signal wavefront are marked by black dashed ellipses to underline their visible regular pattern. **(b)** A typical hit pattern for pure thermal noise.

### A. Thermal noise filtering

Thermal noise filtering is performed with the time sequence filter, developed for the close-to-cubical ARA station geometry. Further details about a first version of the method, described below, can be found in [29].

The algorithm works in three steps. First, a so-called energy envelope is calculated for each recorded waveform and a dynamic signal threshold is set. Then, for any signal with energy above this given threshold, a hit is recorded for the given antenna at that threshold-crossing time. In this way, hit patterns are generated for each event which, in the third step, are checked for consistency with incoming planar radio waves.

The “energy” envelope is in principle calculated as the RMS of a sliding 5 ns time window of the voltage data

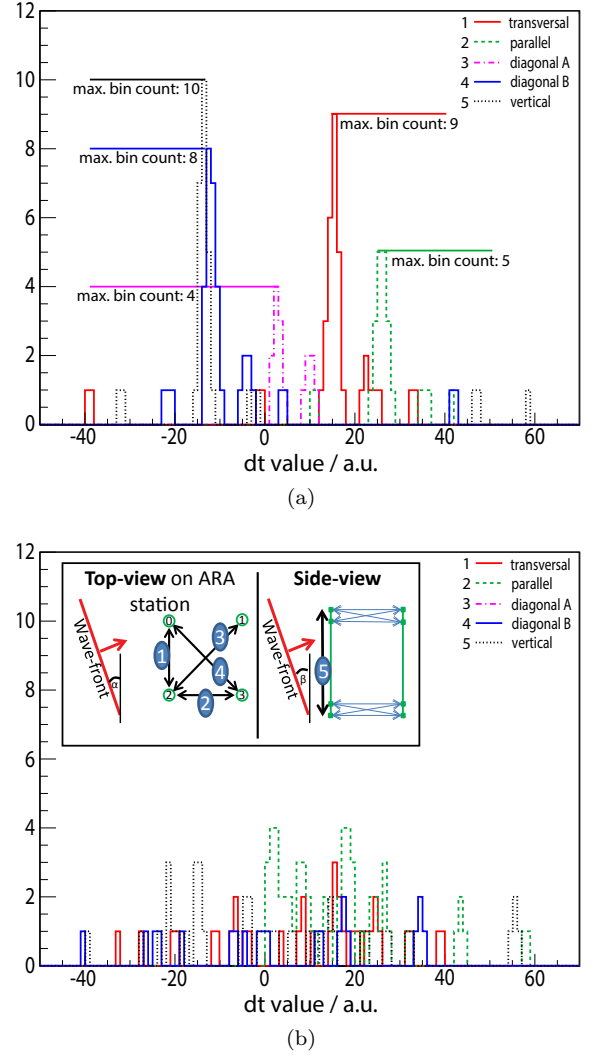


Figure 15. **(a)** The hit time differences in histograms for each of the five geometrical groups for the event shown in Figure 14(a). The pair groups of the histograms are schematically shown as inset in the bottom plot. The quality parameter here ( $QP$ ) = 1.6. **(b)** The hit time difference histograms for the noise event shown in Figure 14(b). In this second case the quality parameter equals 0.5.

to enhance the signal-to-noise ratio. For each event and antenna channel a threshold is defined as  $\mu_E + 4 \cdot \sigma_E$ , with  $\mu_E$  the average and  $\sigma_E$  the RMS of the full energy envelope of a waveform. Whenever an envelope crosses the threshold, a hit is recorded for the given channel with a coarse timing precision of 5 ns. The hits of all channels taken together form a hit pattern (Figure 14).

In the next step, pairs are formed from antennas at roughly the same depth (horizontal pairs) and antennas on the same string (vertical pairs). For pairs with the same geometrical orientation, the time difference, divided by the antenna distance, is filled into a common histogram as shown in Figure 15. This figure illustrates how radio signal patterns and thermal noise patterns are

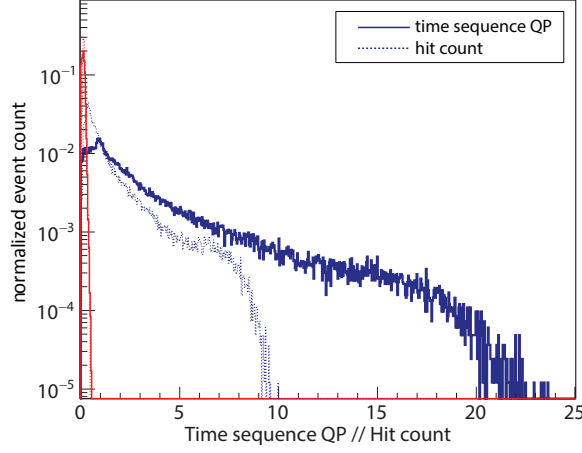


Figure 16. The quality parameter  $QP$  (solid line) compared to a simple count of all hits in a pattern as they appear in the example in Figure 14 (dashed line) for simulated neutrinos with energies between  $10^{16}$  eV and  $10^{21}$  eV (**blue**) and thermal noise events (**red**). All values are scaled to cumulatively reach 99% in both noise distributions at the same X value. The distributions are normalized to the total event count.

finally being separated in the presented algorithm. In total there are five groups of pairs with the same geometrical orientation. For an incoming plane wave these histograms are expected to show a strong peak while they should be a flat distribution for thermal noise. The normalized sum of the maximum bin counts from each histogram is used as the time sequence quality parameter ( $QP$ ), to distinguish incoming wavefronts from thermal noise.

The noise rejection power of this filter is shown in Figure 16 for simulated neutrinos between  $10^{16}$  eV and  $10^{21}$  eV. In the range between  $10^{18}$  eV and  $10^{19}$  eV, 92% of neutrino signals are kept at 99.9% noise rejection. The actual cut has to be tightened to provide adequate thermal noise rejection for the full data sample. However, as will be shown, the signal efficiency remains high.

## B. Vertex reconstruction

After having separated impulsive radio signals from thermal noise, we use a directional vertex reconstruction to distinguish neutrino-induced emission from anthropogenic noise. Here, we use the fact that man-made signals will reconstruct to the surface while only neutrino signals originate from within the ice itself. Furthermore, signals generated above the ice undergo refraction at the ice air boundary. Under the assumption of an index of refraction of 1.755 at the antennas, the critical angle at this interface can be calculated to be  $35^\circ$  and events produced in air are thus limited to a zenith angle between  $90^\circ$  and  $55^\circ$  as viewed in-ice from the ARA stations. Events which are generated directly at the ice boundary, for example by driving vehicles, will arrive with a minimal an-

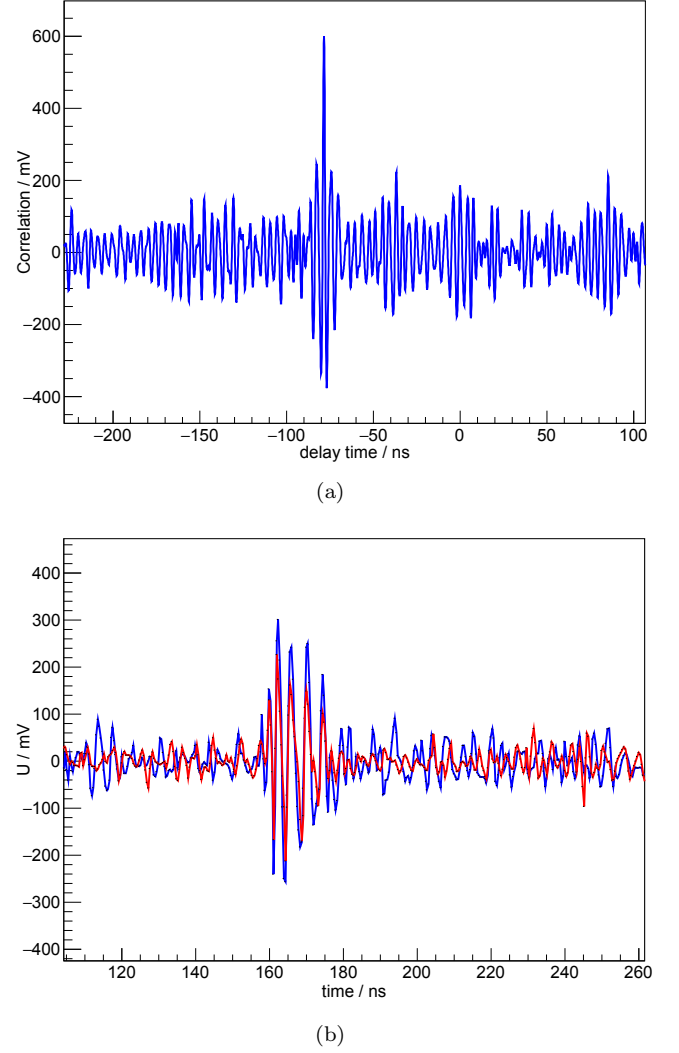


Figure 17. (a) The cross-correlation graph for a calibration pulser signal using waveforms measured in two different antennas. (b) The two recorded waveforms after a shift by the time of maximum correlation  $dt = -78.4$  ns.

gle of roughly  $40^\circ$ . This is, however, not a concern for winter running, when on-ice activities are minimized.

Background radio pulses from cosmic ray air showers, can mainly be emitted from above the ice or as transition radiation from particle bunches at the ice-air boundary [30]. For the ARA stations they will appear in the same angular region as the anthropogenic background described above. In the background estimation they will be summarized as surface events. Only penetrating high energy muon bundles might be able to generate dense enough cascades in the deep ice via catastrophic energy loss to produce detectable radio signals. Studies of UHE neutrinos predict neutrino fluxes to be roughly 100 times smaller than the cosmic ray flux at  $10^{18}$  eV [31]. Furthermore, a study of the energy loss of muon bundles in South Pole ice below 1450 m indicates that at such a primary cosmic ray energy the probability for an energy

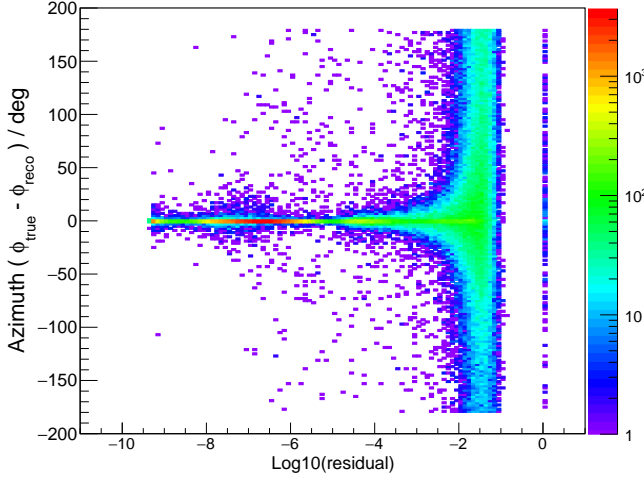


Figure 18. The dependence of the azimuthal reconstruction on the residual (Equation 10). The Y-axis indicates the difference between the reconstructed angle and the true angle for 165000 simulated neutrino events with energies between  $10^{16}$  eV and  $10^{21}$  eV. Events with a high residual triggered the detector but do not contain strong enough signal to be properly reconstructed and are likely thermal in origin.

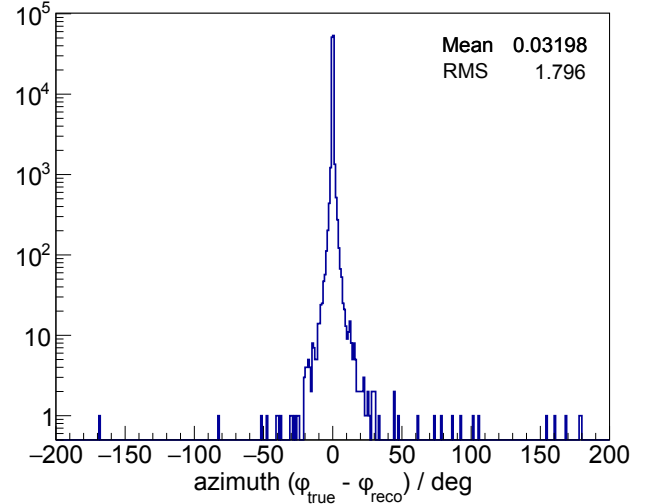
loss of  $10^{16}$  eV over 5 m, the lower end of the ARA sensitivity, is of less than  $10^{-6}$  [32]. This evidence makes us confident that the background expected from muon bundles is small compared to neutrino signals. The actual amount of background, produced by such muon bundles in the ARA detector is currently under investigation.

The reconstruction algorithm developed for this analysis is based on a system of linear equations, formed from the signal arrival times on the different antennas. In the ARA stations relative arrival time differences can be measured using the cross-correlation  $g$  between two antenna waveforms  $f_1$  and  $f_2$  (Figure 17):

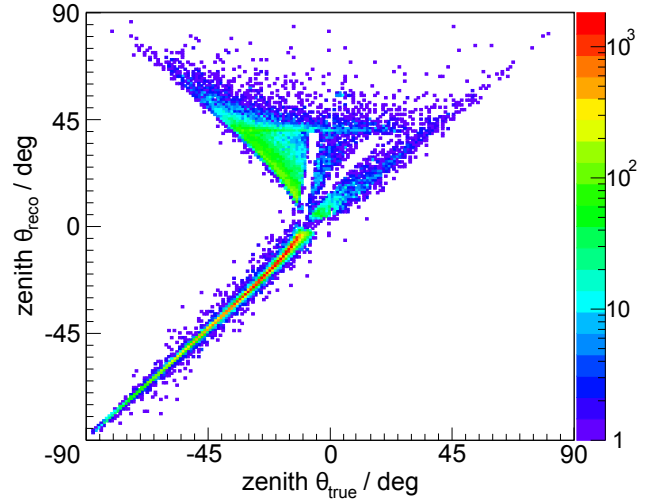
$$g(t) = f_1 \star f_2 = \mathcal{F}^{-1}((\mathcal{F}(f_1))^* \cdot \mathcal{F}(f_2)), \quad (6)$$

where  $\mathcal{F}$  stands for the Fourier transform of a given function. The maximum of the correlation graph should occur at the delay time between the two input signals. With this method, a timing precision of 100 ps on average can currently be achieved in ARA (see Appendix A).

In principle, the time differences from all possible pairs can be used in the reconstruction. However, to exclude antennas that did not register a signal waveform from the algorithm, the maximum correlation amplitude in the correlation graph is used as a selection criterion for good antenna pairs. For a pair to be selected, the correlation amplitude has to cross a dynamic threshold adapted to the overall signal amplitude in an event, but at least  $1/70$  of the product of the integrated power of the two correlated waveforms. All pairs passing the threshold are initially used in the reconstruction prior to a more refined channel pair selection performed in further steps, which is based on quality criteria applied to the outcome of the reconstruction. With the time differences found for good



(a)



(b)

Figure 19. Simulated neutrino vertices reconstructed in azimuth and zenith angle with all quality criteria applied. (a) The difference between reconstructed and true azimuth. (b) The reconstructed zenith angle plotted as a function of the true zenith angle of each event.

antenna pairs, a system of equations is set up, using the equality between the distance to the signal source and the measured travel time:

$$c^2(t_v - t_i)^2 = (x_v - x_i)^2 + (y_v - y_i)^2 + (z_v - z_i)^2, \quad (7)$$

where  $t_v$  is the time of emission at the vertex,  $t_i$  the time of reception by the antenna  $i$  and  $x, y$  and  $z$  the respective spatial coordinates. The speed of light  $c$  is assumed to be constant and equal to the average speed at the station depth  $c = 0.3/1.755$  m/ns (from [20]). The changing index of refraction with depth is not taken into

account in this reconstruction, which has an influence on the zenith reconstruction precision. This, as will be shown, is however not dramatic for the efficiency of the analysis.

When subtracting this relation for pairs of antennas, and after some reordering, one can obtain for each pair of antennas  $i$  and  $j$ :

$$\begin{aligned} \mathbf{x}_v \cdot 2x_{ij} + \mathbf{y}_v \cdot 2y_{ij} + \mathbf{z}_v \cdot 2z_{ij} - \mathbf{t}_{v,ref} \cdot 2c^2 t_{ij} \\ = r_i^2 - r_j^2 - c^2(t_{i,ref}^2 - t_{j,ref}^2). \end{aligned} \quad (8)$$

Here, the index  $ij$  indicates the difference between the values of a certain parameter for antennas  $i$  and  $j$ , the parameter  $r$  denotes the distance to the center of the coordinate system and the index  $ref$  indicates a reference antenna for which the signal arrival time is set to be  $t_0 = 0$ . This relation is used to set up a system of equations, linear in the vertex coordinates and emission time, represented by the matrix equation

$$\mathbf{A}\vec{v} = \vec{b}, \quad (9)$$

with  $\vec{v}$  containing the vertex coordinates and emission time and the matrix  $\mathbf{A}$  and the vector  $\vec{b}$  offsets and arrival time differences. It should be noted that this approach is similar to Bancroft's solution of GPS equations, described in [33]. The solution of this equation can be obtained using matrix decomposition tools [34, 35]. It is thus not seed-dependent and very fast, which allows us to perform several thousand reconstructions per second. Their precision and stability depends strongly on the precise knowledge of the relative antenna positions and possible time offsets between their recorded signals, which can be caused by cables or other electronic components. A calibration of the station geometry and systematic time delays between antenna waveforms has been presented in Section II C. For each reconstruction, a residual is calculated as

$$res = \left| \frac{\vec{b}}{|\vec{b}|} - \frac{\mathbf{A} \cdot \vec{v}}{|\mathbf{A} \cdot \vec{v}|} \right|^2 \cdot \frac{1}{N_{chp}}, \quad (10)$$

to indicate how well the reconstructed values fit the measured arrival time differences. Based on this residual, the channel pair selection is refined to further exclude noise antenna pairs if they have not been identified in the first step of channel selection.

The residual, alongside with some minor quality parameters, indicates whether a reconstruction is considered as trustworthy or if it can be regarded as having failed. Figure 18 shows the dependence of the azimuthal reconstruction on the residual. For low residuals a high quality reconstruction can be obtained while reconstructions with a residual above  $10^{-2.5}$  appear to point to locations that are broadly distributed in azimuth in relation to the true value. The residual also rejects more thermal noise events in favor of signal events although that is not its main purpose.

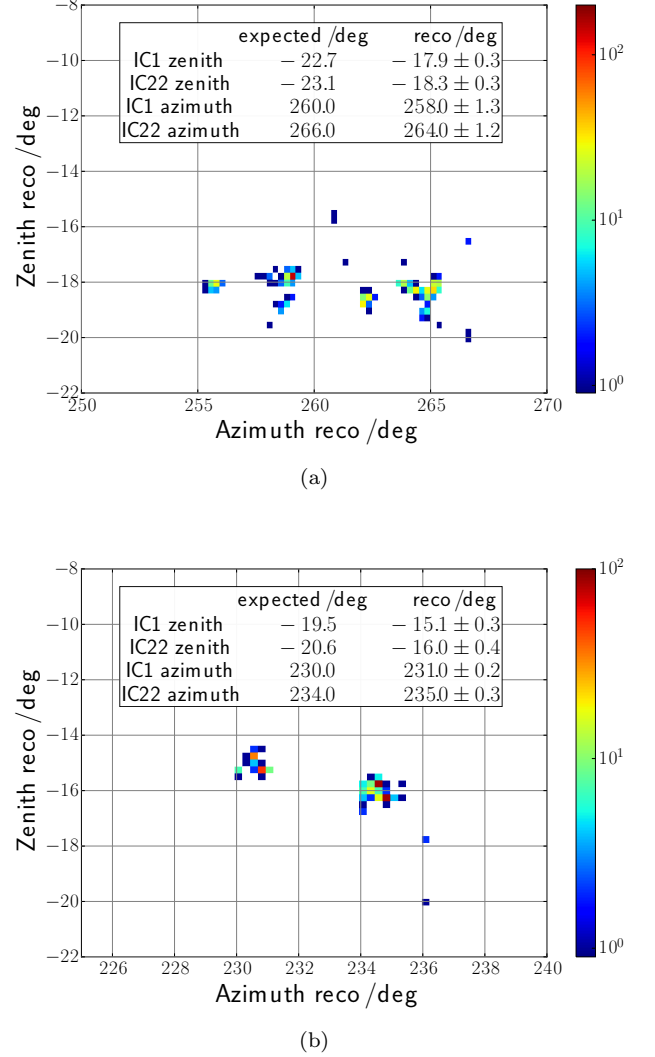


Figure 20. Reconstruction of pulsers deployed in IceCube holes in the deep ice (a) with A2, (b) with A3. The plots include data for the expected positions and the reconstructed positions with their standard deviation. The influence of systematic differences of a few degree between the true and reconstructed angles on neutrino identification is negligible.

The result of reconstructions from a set of simulated neutrinos after application of all reconstruction quality criteria is shown in Figure 19. While for the azimuth reconstruction a precision of better than  $2^\circ$  can be achieved, the zenith reconstruction is significantly degraded by surface reflections and ray-tracing effects. About 30% of the events show behavior which causes the here described reconstruction to fail by several degrees in zenith angle. This causes an efficiency loss due to application of our angular cuts on radio waves coming from the surface, which is, however, not dramatic and only of roughly 6%.

Figure 20 shows the reconstruction of two pulsers deployed at a depth of 1450 m in the ice on IceCube strings

1 and 22 deployed in the final season of IceCube construction. Their distance to the ARA stations is roughly 4000 m. These pulsars are therefore our most neutrino-like calibration tool. The plots show that both pulsars can be reconstructed with a good precision by both stations. In addition to the roof pulser, this is another external source which confirms that the reconstruction algorithms work properly for neutrinos.

### C. Cuts and background estimation

Based on the presented algorithms, three cuts are used to distinguish neutrino signals from thermal and anthropogenic background. Thermal noise has to be reduced by a factor  $10^{-10}$  to reach the goal of ten times less events than the expected number of neutrinos. This can be achieved mainly by requiring a time sequence quality parameter of at least 0.6 to select an event. Further, to make sure that a reconstruction worked properly and to reject the remaining thermal noise, the residual is required to be less than  $10^{-4}$ . In this way only well-reconstructed impulsive radio signals are kept, which can further be reduced by angular cuts. The cut values for the time sequence parameter and the reconstruction residual have not been optimized in a strictly systematic way. There might thus be room for improvement in an analysis which uses the presented algorithms.

Angular cuts are placed around the known locations of calibration pulsers inside the ice and are specific to a given station. In addition to that, a surface cut is applied, rejecting all events reconstructed to a zenith angle of  $\theta > 35^\circ$  for A2 and  $\theta > 40^\circ$  for A3. This cut can be a bit looser for A3 since the reconstruction errors are smaller for this detector. The cut values are chosen for each angular requirement separately, such that each allows less than 0.01 background events to enter the signal sample in the full data set. The number of background events expected to pass a given cut is estimated from the 10% data subset by fitting an adequate Gaussian or exponential function to the tail of an event distribution close to each cut. The best fit parameters and the position of the cut are used to obtain the number of background events expected to leak from the angular region being excluded. The uncertainty on the number of background events is derived from the fit errors. Note that calibration pulser events are normally tagged by the DAQ as calibration events and excluded from the analyzed data sample. However, due to possible miss-tagging, pulser events could leak into the final sample. Therefore, all pulser events are taken into account in the background estimation, even if they are not part of the 10% data subset used for analysis preparation. This is a very conservative estimate but strengthens the analysis against miss-tagged pulser events.

After these cuts, the background expectation for the full data recorded in the year 2013 is  $0.009 \pm 0.010$  for A2 and  $0.011 \pm 0.015$  for A3. The number of neutrinos,

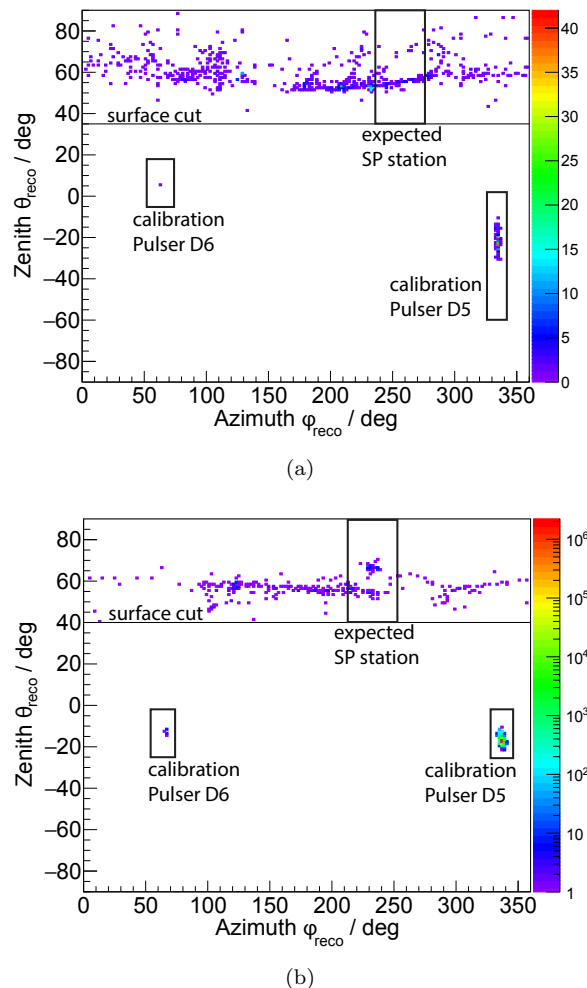


Figure 21. Reconstructed events that passed the thermal noise and reconstruction quality cuts for (a) A2 and (b) A3. The black boxes indicate the angular cut regions around the calibration pulser positions and the black line indicates the surface cut. Events inside the squares and above the surface line are rejected.

expected to be observed by the combined two-station detector from the flux prediction in [31] for a crossover energy from Galactic to extragalactic cosmic ray sources of  $E_{min} = 10^{18.5}$  eV amounts to  $0.11 \pm 0.002(stat)$  events.

## V. RESULTS AND CROSS CHECKS

### A. Results

The results of the above described analysis are summarized in the two sky maps in Figure 21. No events are found outside the angular cut regions which implies that no neutrino candidates have been observed. This agrees with the expectation of 0.1 signal and roughly 0.02 background events in the two stations. The difference between summer and winter activities at South Pole are



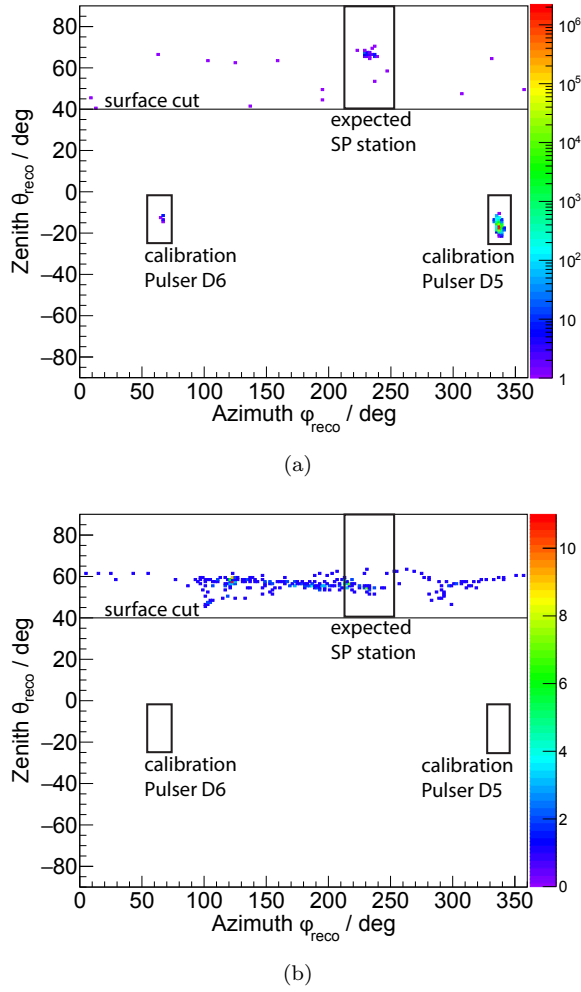


Figure 22. Reconstructed events that passed the thermal noise and reconstruction quality cuts for A3 **(a)** in the austral winter and **(b)** in the austral summer when station activity is maximal. Note that due to a missing event tagging of the calibration pulser in the first months of winter, many events entered the final data sample. This is however accounted for in the final angular cuts of the analysis.

presented in Figure 22, showing the impact of human activities which is, however, limited to surface events.

With this result we can calculate a differential limit on the neutrino flux in the sensitive energy region as shown in Figure 23. For the neutrino energy range between  $10^{18}$  eV and  $10^{18.5}$  eV, the energy where most neutrinos are expected to be observed, the limit is  $E^2 F_{\text{up}}(E) = 3 \times 10^{-6}$  GeV/cm<sup>2</sup>/s/sr.

This limit is calculated as

$$\begin{aligned} E^2 F_{\text{up}}(E) &= E^2 S(E) \cdot \frac{K(E)}{dE} \\ &= ES(E) \cdot \frac{K(E)}{0.5 \cdot \ln(10)}, \end{aligned} \quad (11)$$

where the factor  $K(E)$  is derived with the construction described in [42] as the 90% Poisson confidence limit for

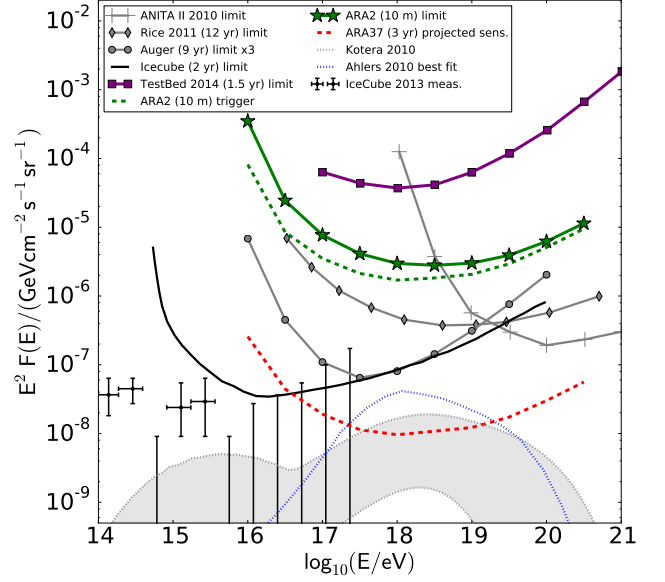


Figure 23. Neutrino limits and sensitivities from various detectors including the 10 months data analysis of the two ARA stations. Systematic errors, as derived in Section VI, have been accounted for in the ARA2 limit. Data for other experiments are taken from [21, 36–40]. The neutrino fluxes are derived in [31] and [41]. See Appendix B for  $EF(E)$  scaling on the y-axis.

no observed events under the expectation of zero background. Systematic errors on the signal efficiency, as described in Section VI, are accounted for in this factor following the method presented in [43] with the improvement proposed in [44]. The error caused by uncertainties on the cross section is not taken into account.  $S(E)$  denotes the sensitivity of the detector which is calculated from the effective areas  $A_{\text{eff}}$  and live times  $T$  of each detector as

$$S(E) = \frac{1}{4\pi \cdot (A_{\text{eff},2} \cdot T_2 + A_{\text{eff},3} \cdot T_3)}. \quad (12)$$

Furthermore, the limit is presented for a logarithmic energy scale with a resolution of  $d\text{Log}_{10}(E) = 0.5$  logarithmic bins. Therefore we obtain:

$$dE = E \cdot \ln(10) d\text{Log}_{10}(E) = 0.5 \cdot E \cdot \ln(10). \quad (13)$$

The resulting limit for two ARA stations after 10 months of operation is not yet competitive with the current best limits from the IceCube detector. In spite of this they show, when projected to the full size of ARA37, that the completed detector is expected to be sensitive to mainstream models for neutrinos from the GZK process.

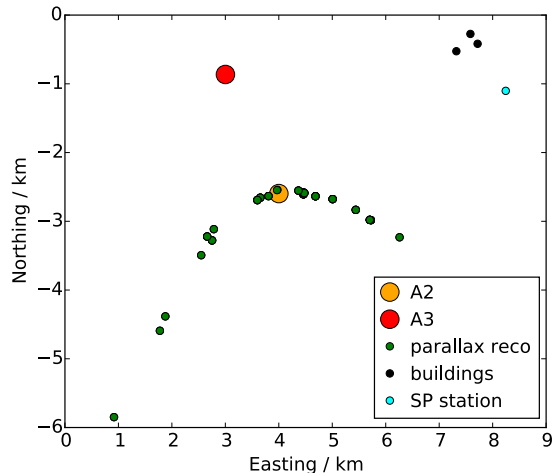


Figure 24. A South Pole map with the two ARA stations and the XY reconstruction of an A2/A3 coincident event series via the parallax method (green dots). The events in this series are distributed over a time of 50 s starting from the rightmost point in the map.

### B. Cross checks

Although the obtained limit with the currently deployed ARA stations is not competitive yet, this first data analysis proves the capabilities of the full ARA detector. Cross checks have been performed with events that are observed coincidentally in both stations to demonstrate that the employed algorithms select impulsive radio signals and that the directional reconstruction works. Events that have passed both the thermal noise and reconstruction quality cuts are considered coincident if they trigger both stations within a time window of 12  $\mu$ s. This time corresponds to the maximal in-ice travel time of signals between the two stations given their separation of 2 km. Sequences of such events, appearing in short time frames of roughly 60 s have been found which show evidence of originating from airplane communication transmitters.

With the azimuthal reconstruction from each station, the XY position of the source can be determined via trigonometric calculations. The crossing point of the two beams pointing to the azimuthal reconstruction of both stations is used as its XY position. This method is in the following referred to as the parallax reconstruction. One particularly interesting event sequence is shown in Figure 24. The positions of the events within this hit series form a smooth track, indicating an emitting object that moves at a speed of several hundred km/h at an increasing height of order 500 m above the ice surface. This track is very useful as a cross check since it passes on top of station A2 which should be evident in zenith reconstruction. In Figure 25, the expected zenith angle

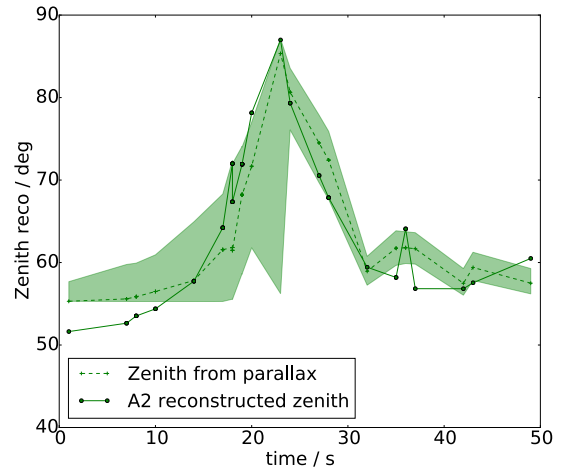


Figure 25. Comparison between the expected zenith from the A2/A3 XY parallax reconstruction (green dashed line) and the reconstructed zenith angle by A2 only (green solid line). Errors from the XY reconstruction, calculated from the errors on the reconstruction of a surface pulser with known position, are shown as a green band.

from the XY position is compared to the zenith reconstruction of station A2, showing good agreement within the error bars.

This agreement and the smoothness of the observed track are evidence that the detector is well-capable of detecting radio signals and that the used analysis tools work properly to identify such signals and reconstruct their source.

## VI. SYSTEMATIC UNCERTAINTIES

The systematic uncertainties of the presented analysis result from errors on the theoretical models of neutrino interactions and radio wave propagation as well as on the calibration of the detector. The error estimation is performed in a similar way as has been described in [21].

The neutrino interaction cross section at the energies of interest above  $10^{16}$  eV is calculated based on measurements at much lower energies and thus subject to large uncertainties. To check the influence of this uncertainty on the effective area of the ARA detector, simulations are run using the upper and lower limits of the cross section estimates from [27]. The effect on the final analysis result can be seen in Figure 26. Especially for the highest energies, this is the dominant uncertainty in the analysis.

A further error results from uncertainty in the radio attenuation length in the South Pole ice sheet. This measurement has been performed using calibrated pulsers, deployed at different depths with the last IceCube strings

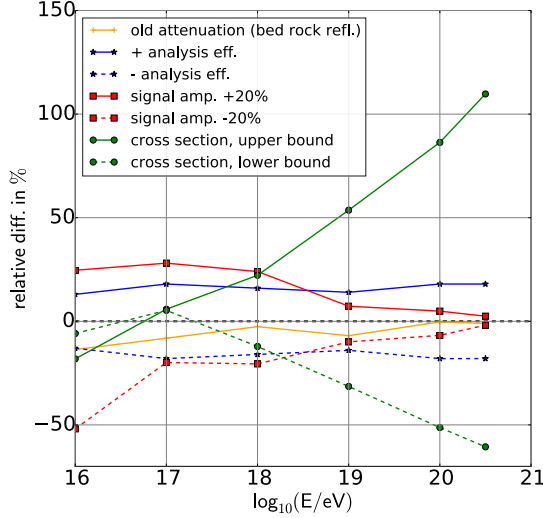


Figure 26. The relative difference in effective area at analysis level, caused by various systematic error sources.

[9]. With the obtained measurements, the local attenuation length at a given depth can be inferred with knowledge of the temperature and density profile of the ice. The difference between this result and an earlier measurement, using the bed rock under the ice as a reflector for radio waves emitted and received at the surface [45], provides a measure of the uncertainty in the attenuation length. The error on the effective area is again obtained by comparing simulations with different sets of parameters. As visible in Figure 26, it contributes only slightly to the final error.

One should note that the uncertainty on the changing index of refraction inside the ice is not a big concern to ARA due to the deep deployment of the stations at 180 m below the ice surface. Below this depth the index of refraction does not change appreciably and approaches the value of 1.78 for the deep ice.

One more important uncertainty relates to the final signal to noise ratio recorded by the signal chain. This depends on the assumed ambient noise, the antenna directivity and transmission coefficient as well as the assumed noise figure. The measured uncertainties have little influence on the final sensitivity. Also the ambient noise temperature does not cause a significant uncertainty. Measurements show that the resulting signal-to-noise ratio of the signal chains varies by, on average, 20% around the expectation from the simulated antennas, ambient noise and the measured noise figures. To estimate the systematic error on the effective area caused by the signal chain uncertainty the overall amplitude of the incoming radio signal is changed by 20% in both directions. Under these conditions, sets of neutrino events are simulated and the analysis is re-run. The presented analysis is nearly exclusively

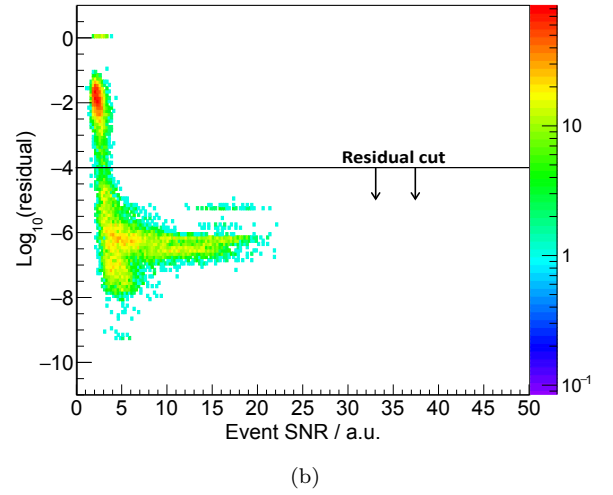
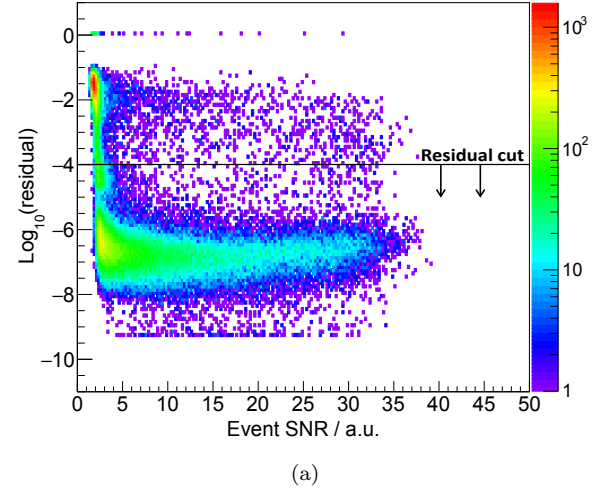


Figure 27. The residual of reconstructed events as function of the  $SNR$  for (a) neutrino simulations in A3 and (b) calibration pulser signals recorded by A3.

based on coarse envelopes of time domain waveforms or time differences, derived from cross-correlation. Therefore, precise knowledge of the frequency response is of secondary importance. Figure 26 shows that the uncertainty on the signal chain calibration has most impact at low energies, when most of the incoming signals are weak and the signal to noise ratio is low. At higher energies, this error loses importance compared to the error on the cross section.

The last estimated uncertainty is the difference in the analysis efficiency obtained from simulated neutrinos and recorded data. The shape of noise and signal waveforms will not perfectly match between simulations and real data. Therefore, the used analysis algorithms are compared between real data from calibration sources and simulated neutrino signals. For this comparison, the signal to noise ratio (**SNR**) is chosen as a simple parameter, independent of the shape of the waveform.

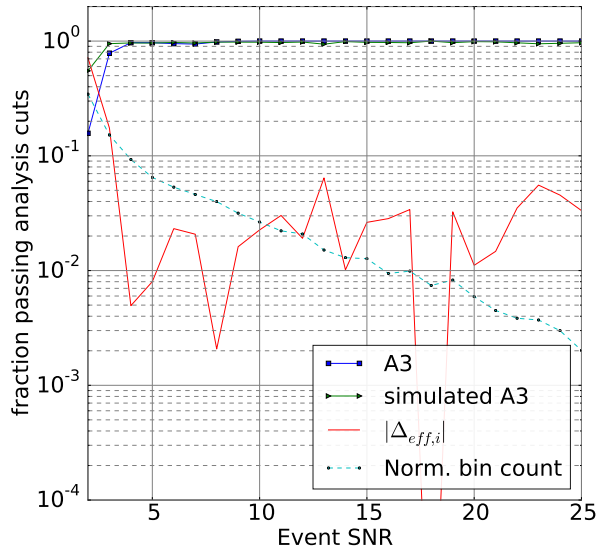


Figure 28. The analysis efficiency of the ARA stations for simulated events (green) with a neutrino energy of  $10^{18}$  eV and for calibration pulser events on A3 (blue), with normalized bin count (cyan) and difference in efficiency (red).

In Figure 27, calibration data from station A3 are compared to simulated neutrino events with energies between  $10^{16}$  eV and  $10^{21}$  eV for one of the two main cut parameters, the reconstruction residual. Generally, the distribution for simulations fits the data very well.

One can compare the analysis efficiency dependence on SNR after separating the simulated neutrinos into single decade energy bins, as shown in Figure 28, and calculate an average difference for neutrinos at each bin energy. This average is weighted by the number of simulated neutrino events in a given SNR bin. As visible in Figure 26, this is a non-negligible contribution to the systematic error. However, with a better knowledge of the detector, simulations will become more precise and this uncertainty can be reduced significantly.

The systematic uncertainties calculated for the number of recorded neutrinos are summarized in Table I.

Table I. The systematic error from various sources on our signal expectation of 0.11 neutrino events for a flux prediction from [31].

Source	positive error	negative error
Cross section	0.037(34%)	0.021(19%)
Attenuation	—	0.005(5%)
Signal Chain	0.018(17%)	0.017(16%)
Analysis efficiency	0.019(17%)	0.019(17%)
TOTAL	0.048(44%)	0.035(32%)

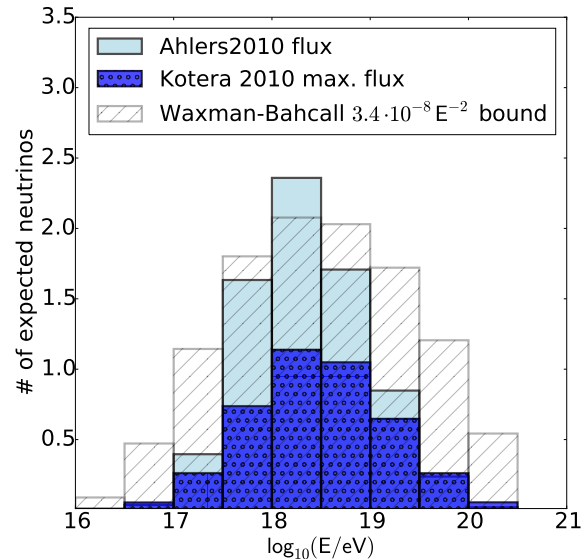


Figure 29. Numbers of neutrinos versus energy in half-decade bins, as expected to be seen with the ARA37 detector, extrapolated from the presented status of trigger and analysis efficiency for the first two stations. The numbers are calculated for 3 different flux predictions which are partly shown in Figure 23 and estimated in [31, 41, 46].

## VII. SUMMARY AND OUTLOOK

The presented analysis of the first data recorded with deep ARA stations shows the capabilities of the planned ARA detector.

We have demonstrated the power of ARA as an UHE neutrino detector through an analysis of data from the two deep stations of ARA currently in operation. Through calibrations, good timing precision and geometrical understanding of the detector has been achieved, which are key factors in the efficiency of detecting radio vertices. Furthermore, initial analysis algorithms have been presented, which show a good efficiency of signal capture at a background reduction by roughly 10 orders of magnitude, at the current trigger settings. Thermal noise can be rejected by simple algorithms to a high level and radio vertices can be reconstructed with an angular precision of a few degrees. This relatively simple reconstruction algorithm is found to be stable in azimuth reconstruction with an RMS of  $1.8^\circ$  and for most cases of zenith reconstruction (see Figure 19) without accounting for ray tracing effects. Improvements and alternatives to the algorithm are currently being developed.

In addition, cross checks show that the used analysis algorithms indeed select radio signals from background and return sensible directional reconstructions.

The presented limit, resulting from one year of data taking, is not yet significant but raises the expectations for the discovery of UHE neutrinos with the full ARA

detector.

The results presented in this paper reflect the status of detector operations in 2013 and of currently available analysis tools. Since then, several improvements have been developed, of which the most important are the following:

- The live time per year has been increased by roughly 30%, thanks to newly developed monitoring tools which allow for quick debugging, in case of downtime due to issues in the detector electronics.
- The trigger and readout windows have been optimized and widened to enhance the detector sensitivity and to render analysis tools, complicated by cutoff signal waveforms, more efficient.
- A PCIexpress bus will be integrated into the DAQ to replace the currently used USB connection. This will allow to record data at a roughly 100 times higher event rate and to lower the trigger threshold, enhancing the neutrino sensitivity.
- New reconstruction algorithms are underway which take ray-tracing effects into account and are therefore expected to show a significant improvement in precision and reconstruction efficiency.
- The detector calibration is under continuous improvement which will especially help to reduce systematic uncertainties on the detector geometry, timing and the signal chain, which consequently improve analysis algorithms like the angular reconstruction.

Figure 29 shows the numbers of neutrinos which are expected to be seen with the ARA37 detector, given the trigger and analysis efficiency for 2013, within 3 years of operation at different energies and from different fluxes. Additionally, an expectation for a power law flux, normalized to the Waxman-Bahcall bound from [46] is plotted to illustrate the response of the detector over a wide range of energy. This figure shows that the planned full ARA detector is a promising candidate for the detection of ultra-high energy neutrinos with the presented status of data taking and analysis. Moreover, we can conclude from the above risen points that this detector shows various possibilities of improvement which will be achieved in the coming years.

## VIII. ACKNOWLEDGMENTS

We thank the National Science Foundation for their generous support through Grant NSF OPP-1002483 and Grant NSF OPP-1359535. We further thank the Taiwan National Science Councils Vanguard Program: NSC 102-2628-M-002-010 and the Belgian F.R.S.-FNRS Grant 4.4508.01. We are grateful to the U.S. National Science

Foundation-Office of Polar Programs and the U.S. National Science Foundation-Physics Division. We would also like to thank the University of Wisconsin Alumni Research Foundation, the University of Maryland and the Ohio State University for their support. Furthermore, we are grateful to the Raytheon Polar Services Corporation and the Antarctic Support Contractor, Lockheed, for field support. A. Connolly would like to thank the National Science Foundation for their support through CAREER award 1255557, and also the Ohio Supercomputer Center. K. Hoffman would likewise like to thank the National Science Foundation for their support through CAREER award 0847658. A. Connolly, H. Landsman and D. Besson would like to thank the United States-Israel Bi-national Science Foundation for their support through Grant 2012077. A. Connolly, A. Karle and J. Kelley would like to thank the National Science Foundation for the support through BIGDATA Grant 1250720. D. Besson and A. Novikov acknowledge support from National Research Nuclear University MEPhI (Moscow Engineering Physics Institute). R. Nichol would like to thank the Leverhulme Trust for their support.

## Appendix A: Calibration of the IRS2 digitizer chip

The IRS2 chip is a custom ASIC for radio frequency applications [47]. It is designed to digitize at a speed of several GS/s at low power consumption of less than 20 mW per channel. These features merit usage of CMOS technology for the implementation of the sampling and digitization steps, as well as utilization of a large analog buffer, which allows for a slow digitization technique without inducing dead time. In the IRS2 chip the data are sampled via a Switched Capacitor Array (SCA) which utilizes finely tuned delay elements to set up a sampling sequence of the input data. These delay elements can differ from their nominal delay width due to process variations during the chip fabrication and have to be calibrated individually. The SCA consists of 128 sampling capacitors per

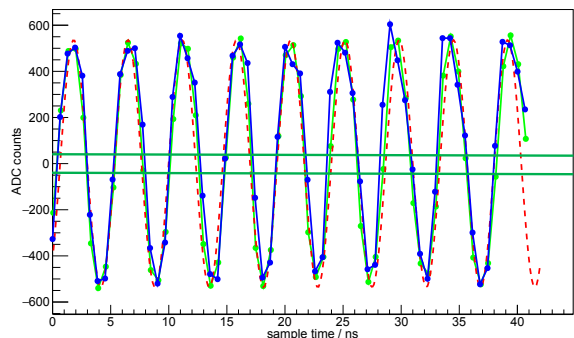


Figure 30. A typical calibration waveform separated by even (blue) and odd (green) samples with a fit waveform (red). The horizontal lines indicate the range for individual sample correction in timing.



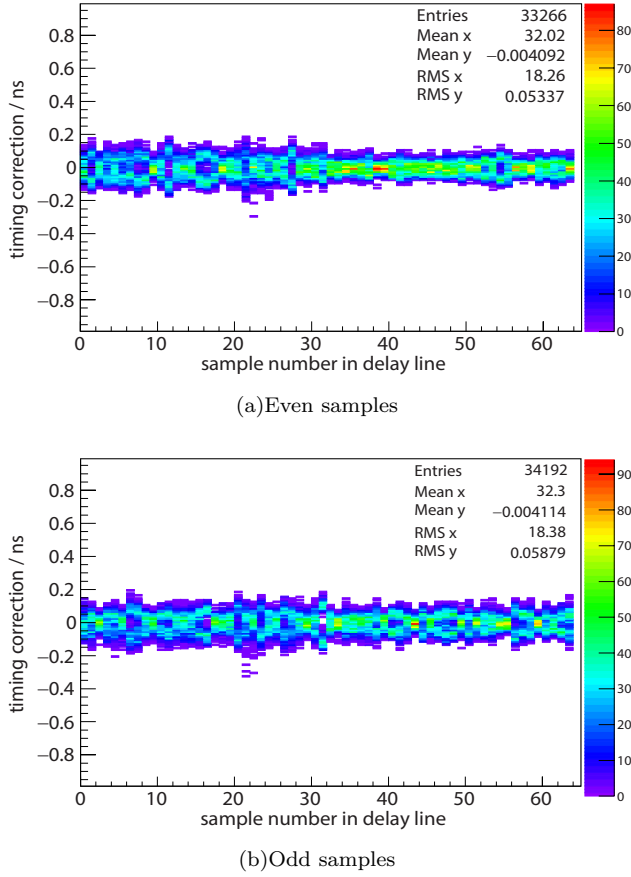


Figure 31. The timing corrections for all delay elements (X-axis) of one channel in station A3, separated by even and odd delay line after several iterations of calibration.

channel, equally divided into even and odd samples on two delay lines and each with a delay element requiring individual calibration in timing. In addition to that the ADC to voltage conversion gain needs to be determined for each of the 32768 buffer elements on each channel to obtain a proper voltage calibration.

For both calibrations, timing and ADC gain, sine waves are recorded and fit to ideal waveforms (Figure 30). The data are recorded in the laboratory with the instrument at the final in-ice temperature of  $-50^\circ\text{C}$ . The calibration is not expected to vary with time.

For the timing, first the fit frequency is compared to the frequency of the input waveform to calibrate the average sampling speed. Then, each individual sample timing is compared to the fit waveform to obtain a correction factor for the given delay element. This correction is applied if samples have an absolute ADC count below 30, thus if the derivative of the sine wave is maximal and the influence of voltage errors are small. Corrections are directly applied and the process is repeated for several iterations until the correction factors converge. Figure 31 shows the final timing corrections needed for samples of a selected channel after several iterations of calibra-

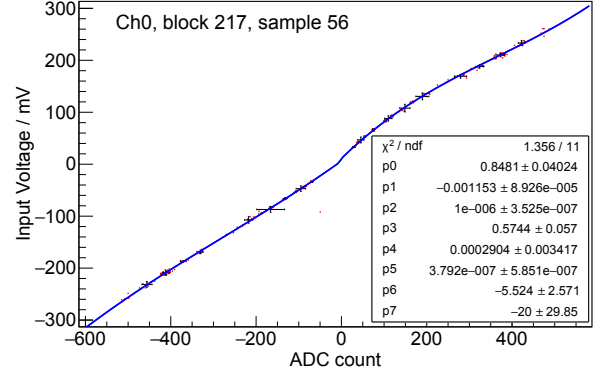


Figure 32. Calibration data for the calculation of the ADC-to-voltage conversion for a single storage sample: Collected data (**red dots**), averaged data (**black points**) with errors, a broken 3rd order polynomial fit to the average data (**blue line**) with fit parameters are shown in the figure.

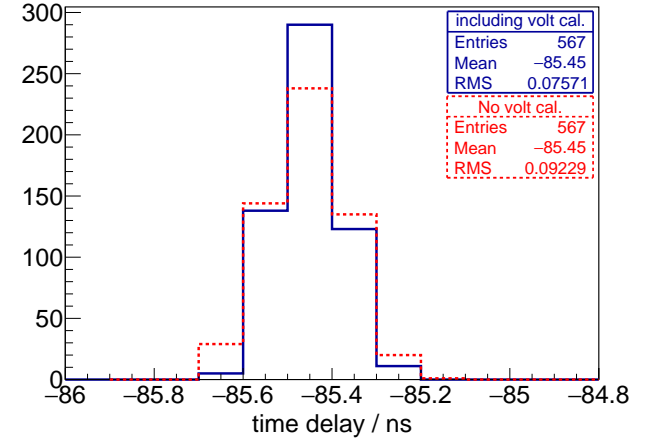


Figure 33. Arrival time difference for a calibration pulser signal on two channels of station A2 after timing calibration (**red**) and the full calibration (**blue**).

tion. One can observe a statistical fluctuation which is however symmetric around zero, which is a sign that all systematic errors have been removed by the calibration. The underlying calibration values are then used to set the correct timing for each delay element. The visible spread of some distributions is connected to a non-linearity in the voltage of the respective sample.

For the voltage calibration, timing-corrected waveforms are used as input. Due to the density of the chip structure, a slight non-linearity and asymmetry around 0 is induced in voltage which depends strongly on the channel number. Furthermore, we need calibration data for about 650000 storage elements per station, which requires a huge data sample. These conditions render classical voltage calibration methods difficult. For the calibration of the ADC to voltage conversion gain of the IRS2, input sine waves of known amplitude and frequency are fit and ADC samples are compared to the fit whenever

its derivative is smaller than 45% of the maximal value. In contrast to the timing calibration, a small derivative is required, this time to minimize the influence of timing errors. Following this procedure a statistically significant sample for each storage element can be collected, using input waveforms over a wide range in amplitude (Figure 32).

Further calibrations which have been performed on the IRS2 chip are a check of

- the frequency response, which could not be determined conclusively with the used data set,
- the temperature dependence of timing and voltage, which appears to be negligible in the temperature range of the ARA experiment.

The main purpose of the calibration is to obtain a good correlation timing between incoming waveforms. Therefore, the calibration is cross checked with calibration pulser waveforms, recorded on different channels. On average, a precision of 100 ps can be achieved (Figure 33), which is entirely adequate for a good vertex angular reconstructions. Determination of the radius of curvature of the incoming wavefront is considerably more difficult with stations of limited size; therefore, for sources more than tens of meters from the station, the range to emission is effectively an unknown to date.

## Appendix B: Neutrino limits with alternative $EF(E)$ scaling

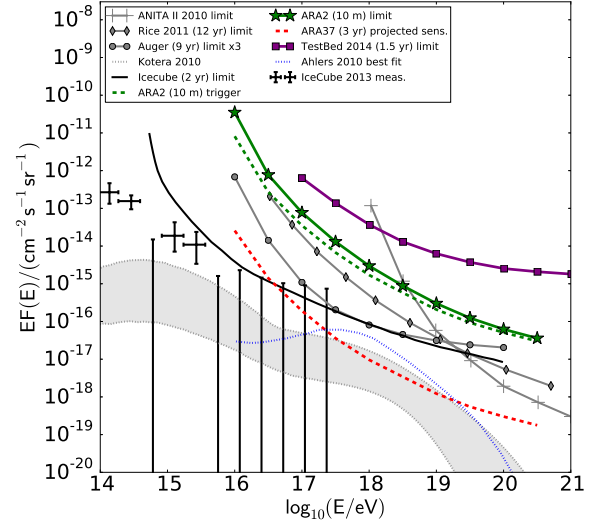


Figure 34. The neutrino limits and fluxes of Figure 23 with an alternative y-axis scaling for convenience.

- [1] K. Greisen, Phys. Rev. Lett. **16**, 748 (1966).
- [2] G. T. Zatsepin and V. A. Kuzmin, JETP Lett. **4**, 78 (1966), [Pisma Zh. Eksp. Teor. Fiz.4,114(1966)].
- [3] V. S. Berezinsky and G. T. Zatsepin, Phys. Lett. **B28**, 423 (1969).
- [4] P. Tinyakov (Telescope Array), *Proceedings, 4th Roma International Conference on Astro-Particle Physics (RICAP 13)*, Nucl. Instrum. Meth. **A742**, 29 (2014).
- [5] J. Abraham *et al.* (Pierre Auger), Phys. Lett. **B685**, 239 (2010), arXiv:1002.1975 [astro-ph.HE].
- [6] D. Allard *et al.*, JCAP **0609**, 005 (2006), arXiv:astro-ph/0605327 [astro-ph].
- [7] M. Ahlers and F. Halzen, Phys. Rev. D **86**, 083010 (2012).
- [8] R. Gandhi, C. Quigg, M. H. Reno, and I. Sarcevic, Astroparticle Physics **5**, 81 (1996).
- [9] P. Allison *et al.* (ARA), Astroparticle Physics **35**, 457 (2012).
- [10] G. A. Askaryan, JETP **41**, 616 (1962).
- [11] G. A. Askaryan, JETP **48**, 988 (1965).
- [12] E. Zas, F. Halzen, and T. Stanev, Phys. Rev. D **45**, 362 (1992).
- [13] J. Alvarez-Muiz and E. Zas, Physics Letters B **411**, 218 (1997).
- [14] D. Saltzberg *et al.*, Phys. Rev. Lett. **86**, 2802 (2001).
- [15] P. W. Gorham *et al.*, Phys. Rev. D **72**, 023002 (2005).
- [16] P. W. Gorham *et al.* (ANITA), Phys. Rev. Lett. **99**, 171101 (2007).
- [17] L. D. Landau and I. I. Pomeranchuk, Dokl. Akad. Nauk SSSR **92**, 535 (1953).
- [18] A. B. Migdal, Phys. Rev. **103**, 1811 (1956).
- [19] P. B. Price *et al.*, Proceedings of the National Academy of Sciences **99**, 7844 (2002).
- [20] I. Kravchenko, D. Besson, and J. Meyers, Journal of Glaciology **50**, 522 (2004).
- [21] P. Allison *et al.* (ARA), Astropart. Phys. **70**, 62 (2015), arXiv:1404.5285 [astro-ph.HE].
- [22] ITU-R, *Radio noise*, Recommendation P.372-11 (International Telecommunication Union, Geneva, 2013).
- [23] D. E. Gary, "Radio astronomy: Lecture 3," <https://web.njit.edu/~gary/728/Lecture3.html>, accessed: 2015-04-09.
- [24] J. A. Shaw, American Journal of Physics **81** (2013).
- [25] "Xfdd documentation," <http://www.remcom.com/xf7> (2015).
- [26] E. S. Hong, A. Connolly, and C. G. Pfendner for the ARA Collaboration, in *33rd International Cosmic Ray Conference (ICRC 2013)*, Rio de Janeiro, Brazil (2013).
- [27] A. Connolly, R. S. Thorne, and D. Waters, Phys. Rev. D **83**, 113009 (2011).
- [28] J. Alvarez-Muñiz, A. Romero-Wolf, and E. Zas, Phys. Rev. D **81**, 123009 (2010).
- [29] T. Meures for the ARA Collaboration, in *33rd International Cosmic Ray Conference (ICRC 2013)*, Rio de Janeiro, Brazil (2013).
- [30] K. D. de Vries, S. Buitink, N. van Eijndhoven,

- T. Meures, A. O’Murchadha, and O. Scholten, (2015), arXiv:1503.02808 [astro-ph.HE].
- [31] M. Ahlers *et al.*, Astroparticle Physics **34**, 106 (2010).
- [32] X. Bai, D. Chirkin, T. Gaisser, T. Stanev, and D. Seckel, in *31st International Cosmic Ray Conference (ICRC 2009) Lodz, Poland, July 7-15, 2009* (2009).
- [33] S. Bancroft, Aerospace and Electronic Systems, IEEE Transactions on **AES-21**, 56 (1985).
- [34] W. H. Press, *Numerical recipes 3rd edition: The art of scientific computing* (Cambridge University Press, New York, 2007).
- [35] “Eigen3 documentation,” <http://eigen.tuxfamily.org> (2014).
- [36] M. Aartsen *et al.* (IceCube), Phys.Rev. **D88**, 112008 (2013), arXiv:1310.5477 [astro-ph.HE].
- [37] P. W. Gorham *et al.*, Phys. Rev. D **82**, 022004 (2010).
- [38] I. Kravchenko *et al.*, Phys. Rev. D **85**, 062004 (2012).
- [39] A. Aab *et al.* (Pierre Auger), Phys.Rev.D (2015), arXiv:1504.05397 [astro-ph.HE].
- [40] M. G. Aartsen *et al.* (IceCube), Phys. Rev. Lett. **113**, 101101 (2014), arXiv:1405.5303 [astro-ph.HE].
- [41] K. Kotera *et al.*, Annual Review of Astronomy and Astrophysics **49**, 119 (2011), <http://dx.doi.org/10.1146/annurev-astro-081710-102620>.
- [42] G. J. Feldman and R. D. Cousins, Phys. Rev. D **57**, 3873 (1998).
- [43] J. Conrad, O. Botner, A. Hallgren, and C. Perez de los Heros, Phys. Rev. **D67**, 012002 (2003), arXiv:hep-ex/0202013 [hep-ex].
- [44] G. C. Hill, Phys. Rev. **D67**, 118101 (2003), arXiv:physics/0302057 [physics].
- [45] S. Barwick, D. Besson, P. Gorham, and D. Saltzberg, Journal of Glaciology **51**, 231 (2005).
- [46] J. Bahcall and E. Waxman, Phys. Rev. D **64**, 023002 (2001).
- [47] G. S. Varner *et al.*, “Specifications for the IceRay Sampler (IRS) ASIC,” [http://www.phys.hawaii.edu/~varner/IRS\\_spec\\_v01.pdf](http://www.phys.hawaii.edu/~varner/IRS_spec_v01.pdf) (2009).